Unified microscopic approach to the interplay of pinned-Wigner-solid and liquid behavior of the lowest Landau-level states in the neighborhood of $\nu=1/3$

Constantine Yannouleas and Uzi Landman

Phys. Rev. B **84**, 165327 — Published 27 October 2011

DOI: 10.1103/PhysRevB.84.165327

Unified microscopic approach to the interplay of pinned-Wigner-solid and liquid behavior of lowest-Landau-level states in the neighborhood of $\nu = 1/3$

Constantine Yannouleas* and Uzi Landman†
School of Physics, Georgia Institute of Technology, Atlanta, Georgia 30332-0430
(Dated: 6 October 2011)

Recently observed microwave resonances in the spectrum of a two-dimensional electon gas under high magnetic fields in the neighborhood of the fractional filling $\nu = 1/3$ were interpreted as signatures of a weakly pinned Wigner solid. Using the rotating-and-vibrating electron-molecule (RVEM) theory [Yannouleas and Landman, Phys. Rev. B **66**, 115315 (2002); Phys. Rev. A **81**, 023609 (2010)], in conjunction with exact diagonalization, a unified microscopic approach is developed for the interplay between liquid fractional-quantum-Hall-effect (FQHE) states and Wigner-solid states in the lowest Landau level (LLL) in the neighborhood of $\nu = 1/3$. In contrast to more traditional treatments, the RVEM theory utilizes a single class of variational wave functions for the description of both the FQHE liquid and Wigner-solid states, and their coexistence.

Liquid characteristics of the FQHE states are associated with the symmetry-conserving rotations and vibrations of the electron molecule. The liquid characteristics, however, coexist with intrinsic correlations that are crystalline in nature, as revealed by the conditional probability distributions. Although the electron densities of the symmetry-conserving LLL states do not exhibit crystalline patterns, the intrinsic crystalline correlations are reflected in the emergence of cusp yrast states in the LLL spectra. These cusp states correspond to fractional fillings in the thermodynamic limit and are the only ones to provide the global ground states of the system. It is shown that away from the exact fractional fillings, weak pinning perturbations (due to weak disorder) may overcome the energy gaps between adjacent global states and generate pinned *broken symmetry* ground states as a superposition of symmetry-conserving LLL states with different total angular momenta. The electron densities of such mixed states (without good angular momentum quantum numbers) exhibit oscillating patterns that correspond to molecular crystallites. These pinned Wigner crystallites represent finite-size precursors of the bulk Wigner-solid state. It is further shown that the emergence of these molecular crystallites is a consequence of the presence of RVEM components in the symmetry-conserving LLL states. In addition, it is shown that the RVEM approach accounts for the Wigner-solid state in the neighborhood of $\nu = 1$, which was also found in the experiments. Utilizing results for sizes in a wide range from $N = 6$ to $N = 29$ electrons, we address the extrapolation to the thermodynamic limit of the energetics of pinned Wigner crystallites, showing development of a crystal of enhanced stability due to contributions of quantum correlations. Furthermore, we address the size evolution of the crystal motifs (culminating in a hexagonal bulk two-dimensional Wigner lattice).

PACS numbers: 73.43.-f, 71.10.Pm, 73.20.Qt

I. INTRODUCTION

In the early 1980's, the widely accepted theorical interpretation of the fractional quantum Hall effect (FQHE) phenomenon[1] was formulated around the antithesis between a new form of quantum fluid respresented by the celebrated Jastrow-Laughlin wave function[2] and the pinned Hartree-Fock Wigner crystal (HFWC) described in the work of Fukuyama and Lee[3] and Maki and Zotos.[4] In the above, the Wigner-crystal (WC) phase has been described[3,4] by broken-symmetry variational wave functions which differ from those used for the quantum liquid.[2]

The seminal paper by Laughlin[2] pointed to two key aspects in favor of the "quantum-fluid" interpretation:

(i) The energy per particle of the HFWC varied smoothly with the filling factor ν in contrast to the experiment. However, Laughlin's wave function corresponded naturally to the major fractional fillings [$\nu = 1/(2p+1)$] that were observed experimentally [as a result of the conservation of its total angular momentum $L = (2p+1)N(N-1)/2$].

(ii) The energy per particle (extrapolated to the thermodynamic limit $N \to \infty$) of the Laughlin-liquid state was substantially lower than that of the Wigner crystal at $\nu = 1/3$. In the context of the major fractions, a crossover[2] to a Wigner-crystal ground state[5] was calculated to occur only for smaller fractional fillings; initially the onset of Wigner-solid ground states had been estimated to occur for fillings $1/11 \leq \nu \leq 1/9$, while later studies[6] predicted crossover already for $1/7 \leq \nu \leq 1/5$.

Based on the above studies, signatures of the Wigner crystal were expected to appear naturally in the range of smaller filling factors, and indeed over the last two decades experimental studies of the Wigner crystal in the lowest Landau level (LLL) seemed to validate the above crossover prediction.[7–10] Furthermore this crossover behavior between liquid (larger major fractions) and crystal (smaller major fractions) was also in agreement with the composite fermion (CF) approach for the liquid states,[11–13] including the modifications of the HF

Wigner crystal referred to as composite fermion Wigner crystals.[13–17] (For an outline of the status of the CF theory for the Wigner crystal, see Sec. VI below.)

In light of the above, the most recent observation[18] of experimental signatures associated with a pinned Wigner crystal in the immediate neighborhood of $\nu = 1/3$ (as well as[18,19] in the neighborhood of $\nu = 1$) represents a rather surprising development. In this paper, motivated by the above recent experimental observations, we further develop the quantal theory of the rotating and vibrating electron-molecule (RVEM) description.[20] The RVEM incorporates liquid and crystalline correlations on an equal footing; it was introduced by us in previous publications[20–24] and was shown[20] to accurately describe the full LLL spectrum. In the RVEM theory, the description of both liquid and Wigner-solid states is achieved within the framework of a single class of variational wave functions (see Refs. 20 and 21). This allows us (see below) to discuss the coexistence of FQHE liquid and Wigner-solid states. Namely, we will show that the application of this theory to the LLL states in the neighbohoods of $\nu = 1/3$ and $\nu = 1$ provides a *unified* microscopic interpretation (i.e., amenable to direct comparisons with exact solutions) pertaining to the emergence of both liquid-like and Wigner-solid behavior. In addressing the emergence of the Wigner crystalline state and its coexistence with the FQHE liquid, it is imperative that quantitative estimates of the energy difference between the liquid and solid states be provided.

The plan of the paper is as follows:

Sec. II presents a brief outline of the RVEM trial functions and shows (in the neighborhood of $\nu = 1/3$) that the liquid characteristics of the LLL states coexist with intrinsic crystalline correlations revealed in the conditional probability distributions [CPDs, see Eq. (9)]. Further insights into the underlying physical reasons for this coexistence are given in Secs. II A and II B, where examples of quantitative analyses of the vibrational content (in terms of RVEM components) of the symmetry-conserving LLL states (obtained through exact diagonalization) are presented.

Sec. III describes (in the neighborhood of $\nu = 1/3$) the effect of weak pinning (experimentally caused by weak disorder[25]) that generates broken-symmetry molecular (Wigner) crystallites manisfested in the electron density (ED) of the two-dimensional (2D) system. These broken-symmetry crystalline states result from the mixing of symmetry-conserving LLL states with different total angular momenta.

Sec. IV shows that the RVEM theory of liquid versus Wigner-crystallite behavior can be extended to the neighborhood of $\nu = 1$.

Our findings are not limited to the case of $N = 6$ electrons (examined in detail in Secs. II, III, and IV); they extend to larger sizes, as well. Indeed Sec. V presents results for sizes in the range from $N = 7$ to $N = 29$ electrons. This section also addresses the extrapolation to the thermodynamic limit of the energetics (energy difference from the liquid FQHE state) of pinned Wigner crystallites, as well as the size evolution of the crystal motifs (culminating in a 2D hexagonal Wigner lattice for $1/N \to 0$).

Sec. VI offers an outline of the status of composite-fermion literature regarding the challenging problem of a Wigner solid in the neighborhood of $\nu = 1/3$.

A summary is given in Sec. VII.

Appendix A recapitulates the remaining analytic expressions needed to define the RVEM trial wave functions presented in Eq. (5). Furthermore, with the insights gained in this paper and the equivalence[20] between the composite-fermion and the RVEM theories, Appendix B shows that intrinsic crystalline correlations are exhibited in the conditional probability distributions of the composite-fermion trial functions in the neighborhood of $\nu = 1/3$. Moreover, Wigner crystallites (showing crystalline electron-density oscillations) are obtained via mixing of CF LLL states through the pinning process introduced in Sec. III.

II. RO-VIBRATING ELECTRON MOLECULE AND THE DESCRIPTION OF LIQUID-TYPE BEHAVIOR

As has been discussed earlier,[26,27] the many-body Hamiltonian ($\mathcal{H}$) of an assembly of N electrons in the LLL is reduced to its two-body interaction (Coulombic) component, i.e.,

$$H_{\rm LLL}^{\rm int} = N\frac{\hbar\omega_c}{2} + \sum_{i=1}^{N}\sum_{j>i}^{N}\frac{e^2}{\kappa r_{ij}}, \tag{1}$$

where $r_{ij} = |\mathbf{r}_i - \mathbf{r}_j|$, κ is the dielectric constant, $\omega_c = eB/(m^*c)$ is the cyclotron frequency, B is the applied magnetic field perpendicular to the plane, and m^* is the effective mass of the electron.

The neutralizing ionic background generates an overall external confinement.[28–33] For high B, the external confinement contributes an additional Hamiltonian term $H_{\rm LLL}^{\rm con}$ (see Sec. III) which influences only the total energies of the LLL states, but not their many-body structure. Its effects do not need to be considered in this section (such consideration will be postponed to Sec. III).

The eigenstates of the Hamiltonian in Eq. (1) have the property that they conserve the total angular momentum $L = \sum_{i=1}^{N} l_i$. This is instrumental in relating the precursor states of the finite system to the thermodynamic filling factors ν via the relation[2,34]

$$\nu = L_0/L, \tag{2}$$

with

$$L_0 = N(N-1)/2. \tag{3}$$

For example, for a system of $N = 6$ electrons, the lowest-energy state with a total angular momentum $L = 45$

is the precursor that corresponds to the $\nu = 1/3$ filling factor in the thermodynamic limit; for $N = 7$ electrons, the corresponding state is the lowest-energy one with $L = 63$.

To determine the eigenstates and eigenenergies of the LLL Hamiltonian in Eq. (1), we employ two complementary approaches:

1. The usual exact diagonalization (EXD) method which employs uncorrelated Slater determinants as the basis for the expansion of the many-body wave function. The number of Slater determinants in the expansion is referred to as the dimension of the EXD. These Slater determinants are made out from the LLL single-particle orbitals

$$u_l(\mathbf{r}) = (2\pi 2^l l!)^{-1/2} r^l e^{il\phi} e^{-r^2/4}, \tag{4}$$

with lengths in units of the magnetic length $l_B = \sqrt{\hbar/m^*\omega_c}$.

2. The rotating-and-vibrating electron-molecule diagonalization (RVEM-diag) which was introduced in Ref. 20. This method employs the technique of diagonalizing the LLL Hamiltonian in Eq. (1) by expanding the many-body wave function in a correlated basis constructed with the general rovibrational electron-molecule (RVEM) trial functions (within a normalization constant)

$$\Phi_L^{\rm RVEM} = \Phi_{\mathcal{L}}^{\rm REM}(n_1, n_2, \ldots, n_r) Q[\Lambda]|0\rangle, \tag{5}$$

where

$$Q[\Lambda] \equiv Q_{\lambda_1}^{m_1} Q_{\lambda_2}^{m_2} Q_{\lambda_3}^{m_3}, \tag{6}$$

with $\Lambda = \lambda_1 m_1 + \lambda_2 m_2 + \lambda_3 m_3$. The number of RVEM states in the expansion is referred to as the dimension of the RVEM-diag; for a given L, this is much smaller[20] than the dimension used in the EXD.

The index REM stands for "rotating electron molecule." [The terms Wigner molecule (WM) and rotating Wigner molecule (RWM) are also often used; they are equivalent to electron molecule (EM) and REM, respectively.] Here and in the following, $(n_1, n_2, \ldots, n_r)$ denotes an N electron configuration consisting of concentric polygonal rings, with n_1 electrons in the innermost ring, n_2 electrons located in the second inner ring, ..., and n_r electrons on the outermost ring; $N = \sum_{i=1}^{r} n_i$. The purely rotational (vibrationless) components $\Phi_{\mathcal{L}}^{\rm REM}(n_1, n_2, \ldots, n_r)$ are associated with the cusp LLL states (see Fig. 1) and have been described in detail in Refs. 20–22, and 24 (see brief description in Appendix A). The general RVEM wave function in Eq. (5) is a product that combines rotations with vibrational excitations, the latter being denoted by Q_λ^m, with λ being an angular momentum; the superscript denotes raising to a power m. Both $\Phi_{\mathcal{L}}^{\rm REM}$ and $Q[\Lambda]$ are homogeneous polynomials of the complex-number particle coordinates $z_1, z_2, \ldots, z_N$, of order $\mathcal{L}$ and Λ, respectively. The total angular momentum $L = \mathcal{L} + \Lambda$. $Q[\Lambda]$ is always symmetric in these variables; $\Phi_{\mathcal{L}}^{\rm REM}$ is anti-

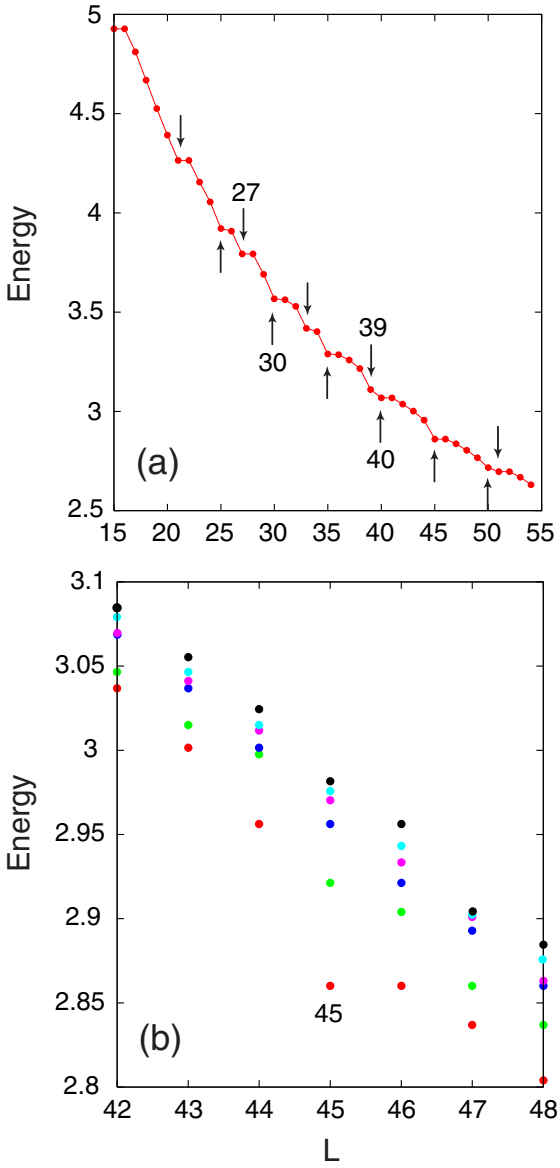

FIG. 1. (Color online) Exact-diagonalization energies for $N = 6$ LLL electrons. Only the Hamiltonian term containing the two-body Coulomb interaction [see Eq. (1)] was considered. (a) LLL yrast states in the range $15 \le L \le 55$. The cusp states of the yrast line are marked by arrows. All the cusp states correspond to either a (1,5) (upward arrows) or to a (0,6) (downward arrows) Wigner-molecule ring configuration.[22,24,37] The cusp at $L = 45$ occurs for both the $(1, 5)$ and $(0, 6)$ Wigner-molecule configurations. (b) The six lowest-in-energy states of the LLL spectrum in the immediate neighborhood of the magic angular momentum $L = 45$ ($\nu = 1/3$). Energies in units of $e^2/\kappa l_B$. The zero of the energy scale correspond to $N\hbar\omega_c/2$.

symmetric (electrons are fermions). $|0\rangle$ is a product of Gaussians

$$|0\rangle = \exp(-\sum_{i=1}^{N} z_i z_i^*/2), \quad (7)$$

which is usually omitted from the notation.

The vibrational excitations Q_λ are given[35,36] by the symmetric polynomials:

$$Q_\lambda = \sum_{i=1}^{N} (z_i - z_c)^\lambda, \quad (8)$$

where z_c is the coordinate of the center of mass and $\lambda > 1$ is an integer positive number.

As was shown in Ref. 20, the RVEM-diag reproduces the EXD results to within arbitray precision. In this paper, we are not focussing on this numerical aspect. Rather we will use the RVEM-diag to analyze the extent that the vibrational degrees of freedom contribute to the exact wave functions in the neighborhood of $\nu = 1/3$, in addition to (and beyond) the vibrationless REM (the REM contibution by itself was studied in earlier publications,[22,23] and naturally only for the exact fractional filling $\nu = 1/3$). The importance of the vibrational components derives from the fact that the Laughlin trial functions (as shown in Ref. 20), as well as the composite-fermion[11,13] ones (see Appendix B), are expandable in the RVEM basis. This suggests an equivalent description of the "liquid character"[12] of the LLL states within the framework of our quantal RVEM theory. Namely, states with a larger weight of rotational-symmetry-preserving vibrational components exhibit enhanced liquid-like character.

In the RVEM approach, the liquid state of the rotating and vibrating molecule is characterized by an azimuthally uniform liquid-like electron density (consistent with the fact that the RVEM wave functions are eigenstates of the total angular momentum). Nevertheless crystalline correlations are manifested in the CPDs, defined as

$$P(\mathbf{r}, \mathbf{r}_0) = \langle \Phi_L | \sum_{i \neq j} \delta(\mathbf{r}_i - \mathbf{r}) \delta(\mathbf{r}_j - \mathbf{r}_0) | \Phi_L \rangle, \quad (9)$$

where $\mathbf{r}_0$ is a fixed point in the intrinsic frame of reference of the rotating molecule. The CPD gives the probability of finding an electron at position $\mathbf{r}$ given that another one is located at $\mathbf{r}_0$.

In this respect, as discussed in Sec. III of Ref. 23, the rotating/vibrating electron molecule contrasts with the *nonrotating* (static) Wigner molecule familiar from unrestricted Hartree-Fock theories, which does not preserve the total angular momentum. As a result the static Wigner molecule exhibits crystalline patterns in the electron density, and thus it is the proper finite analog of the bulk two-dimensional classical Hartree-Fock Wigner crystal (considered in the early paper of Maki and Zotos[4]) and of its composite-fermion extension[14] (composite-fermion Wigner crystal, CFWC). In the RVEM approach, behavior similar to a Wigner crystal is induced through pinning, as will be elaborated in Sec. III.

TABLE I. Participation weights (sum of coefficients squared) of different subspaces to the RVEM-diag wave function for $N = 6$ and $L = 45$. The total dimension of the RVEM-diag space considered is 44 (149 being the upper limit for the full TI subspace). The symbol $\Phi_{\mathcal{L}}^{\rm REM}(n_1, n_2)Q[\Lambda]$ ($L = \mathcal{L} + \Lambda$) denotes the subspace spanned by all the vibrations considered of the form $Q[\Lambda] \equiv Q_{\lambda_1}^{m_1} Q_{\lambda_2}^{m_2} Q_{\lambda_3}^{m_3}$ with $\Lambda = \lambda_1 m_1 + \lambda_2 m_2 + \lambda_3 m_3$

RVEM subspace	Dimension	Weight
$\Phi_{45}^{\rm REM}(1,5)$	1	0.4477
$\Phi_{40}^{\rm REM}(1,5)Q[5]$	2	0.2344
$\Phi_{35}^{\rm REM}(1,5)Q[10]$	10	0.1490
$\Phi_{30}^{\rm REM}(1,5)Q[15]$	20	0.0912
$\Phi_{45}^{\rm REM}(0,6)$	1	0.0630
$\Phi_{39}^{\rm REM}(0,6)Q[6]$	5	0.0120
$\Phi_{33}^{\rm REM}(0,6)Q[12]$	5	0.0027

We return now to the description of LLL states in the neighborhood of $\nu = 1/3$ having a good angular momentum L. In the context of precursor states in a finite system, Fig. 2 displays EXD results (for electron densities, top row, and CPDs, bottom row) for three characteristic yrast states in this neighborhood. Specifically we consider $N = 6$ electrons in the LLL with total angular momenta $L = 45$ ($\nu = 1/3 = 0.333$), 47, and 50. The EXD electron densities [Fig. 2(a-c)] are azimuthally uniform, in consonance with the quantum fluid picture of the LLL states. In contrast, for all three cases, the EXD calculated CPDs [Fig. 2(d-f)] exhibit crystalline correlations reflecting the predominance of the (1,5) classical isomer[38,39] in the intrinsic frame of a rotating molecule.

The crystalline-like EXD-calculated CPDs for cusp states (here for $L = 45$ and $L = 50$) have been reported in many earlier studies (see, e.g., Refs. 22, 23, 40–43). Our EXD calculations (case of $N = 6$ with $L = 47$ in Fig. 2 and results for other N's and L's reported in Ref. 20) demonstrate that the intrinsic crystalline correlations are present in all states comprising the LLL spectra.

The degree of crystallinity (particle localization) in the CPDs of Fig. 2 varies from one case to the other. This is due to the different weight of the vibrational modes Q_λ^m in comparison to that of the vibrationless REM component [see Eq. (5)]. Naturally, a larger vibrational component in the EXD wave function results in reduced particle localization and in a relative enhancement of the liquid character of the LLL state. It is instructive to analyze the vibrational content of the LLL states in detail with the help of the RVEM theory. As illustrative examples, we consider below the cases of $N = 6$ electrons with $L = 45$ ($\nu = 1/3$), which is an yrast cusp state) and $L = 47$ (an yrast non-cusp state); see Fig. 1.

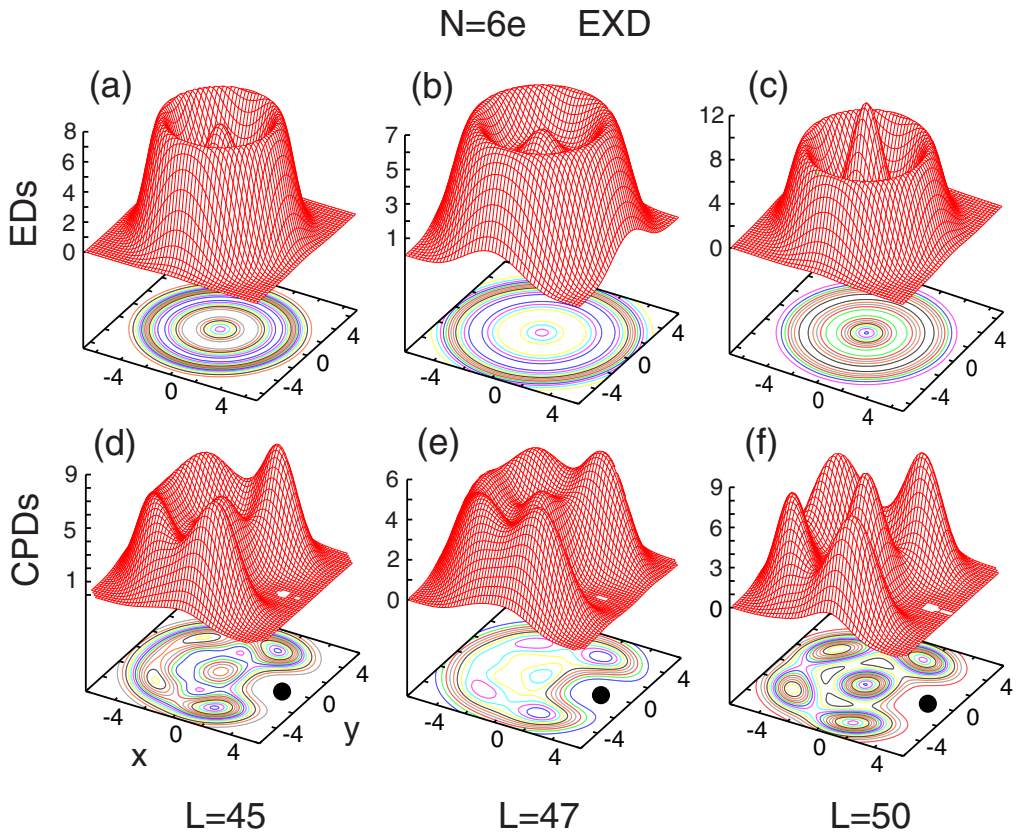

FIG. 2. (Color online) EXD electron densities (EDs, top row) and CPDs (bottom row) in the neighborhood of $\nu = 1/3$ for $N = 6$ LLL electrons, and for angular momenta (from left to right) $L = 45$ ($\nu = 0.333$), 47, and 50. The solid dots denote the position of the fixed point. All three CPDs reveal the predominance (to various degrees) of the (1,5) molecular configuration. The units for the vertical axes in the CPD panels are arbitrary, but the same for all CPD frames here and throughout the paper. Lengths in units of l_B. The ED units are in $10^{-2}l_B^{-2}$. EDs are normalized to the number of particles, N.

A. The case $N = 6$ with $L = 45$ ($\nu = 1/3 = 0.333$)

For $N = 6$ and $L = 45$, the dimension of the EXD Hilbert space is 1206; that is the number of uncorrelated Slater determinants built out of the harmonic-oscillator states $u_l(\mathbf{r})$ [see Eq. (4)]. The translationally invariant[20] (TI) subspace spanned by the RVEM wave functions has a much smaller dimension of 149. Here we analyze RVEM-diag results (see TABLE I) for a smaller RVEM basis of dimension 44; this suffices to yield a many-body yrast state having an 0.990 overlap with the EXD wave function and an energy relative error of 0.141% referenced to the EXD energy (i.e., an energy of 2.864187 $e^2/\kappa l_B$ compared to the EXD energy of 2.860151 $e^2/\kappa l_B$).

The state with $L = 45$ is a cusp state. As a result the RVEM component with highest contribution is expected to have the form of a pure (vibrationless) $\Phi_{45}^{\rm REM}(1,5)$, given that the (1,5) molecular configuration is predominant in the corresponding EXD-calculated CPD [see Fig. 2(d)]. This expectation is confirmed by the RVEM-diag results in TABLE I, where the participation weight (coefficient squared) of this $\Phi_{45}^{\rm REM}(1,5)$ component is listed as 0.4477. We note that in total, including the vibrational components, the (1,5) isomer contributes the most with a participation weight of 0.9223, while the contribution of the (0,6) isomer is only 0.0777.

In Figs. 3(a) and 3(b), the CPD of $\Phi_{45}^{\rm REM}(1,5)$, which is the largest component in the RVEM-diag at $L = 45$, is compared with the CPD associated with the RVEM diagonalization for the maximum expansion (44 RVEM states) considered in TABLE I. The CPD of the pure vibrationless component [Fig. 3(a)] displays a (1,5) isomeric configuration with largest radial and azimuthal variations. The importance of the additional vibrational modes [containing the $Q[\Lambda]$ factors] in bringing a close agreement with the EXD-calculated CPD is apparent [compare Fig. 3(b) with the EXD-calculated CPD in Fig. 2(d)].

For $L = 45$ ($\nu = 1/3$ for $N = 6$), it is natural to compare the behavior of RVEM-diag wave function (with 44 RVEM states, see TABLE I) with that of the Laughlin trial function,[2,13,23] in particular due to the fact that the corresponding energies differ only in the 4th decimal point. Indeed the Laughlin-state energy is 2.86440 $e^2/\kappa l_B$ compared to the RVEM-diag energy of 2.864187 $e^2/\kappa l_B$; this translates to a relative error of 0.148% for

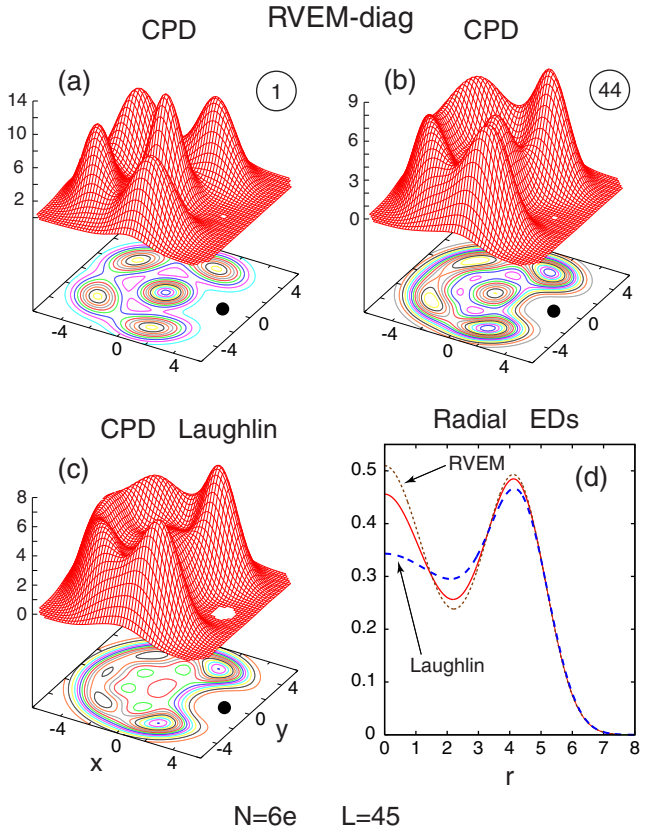

FIG. 3. (Color online) (a-b) RVEM-diag CPDs for the cusp yrast state with $N = 6$ LLL electrons, and $L = 45$ (corresponding to $\nu = 1/3$). (a) CPD with only one RVEM state [namely, $\Phi_{45}^{\rm REM}(1,5)$ with the largest participation, see TABLE I] included in the RVEM basis. (b) The CPD corresponding to the largest number of RVEM states considered in TABLE I. (c) The corresponding CPD for the Laughlin wave function. (d) The radial densities $\rho(r)$ for the EXD (solid line, online red), RVEM-diag (with 44 states, see TABLE I; dotted line, online brown), and Laughlin (long dashed line, online blue) wave functions. The solid dots in (a-c) denote the position of the fixed point. The CPD in (b) exhibits only minor differences from the EXD-calculated CPD in Fig. 2(d). The circled numbers in (a,b) denote the number of states included in the RVEM expansion. The units for the vertical axes in the CPD panels are arbitrary, but the same for all CPD frames here and throughout the paper. Lengths in units of l_B. The units of the vertical axis in (d) are l_B^{-2}. The radial densities are normalized as $\int_0^\infty \rho(r) r dr = N$.

the former compared to 0.141% for the latter.

To proceed in more depth with this comparison, we display in Fig. 3(c) the CPD for the Laughlin state. It is apparent that the Laughlin CPD deviates from the CPD associated with the EXD calculation [Fig. 2(d)] to a larger extent than the RVEM-diag one [Fig. 3(b)]; e.g., the central hump is significantly attenuated in the Laughlin-state CPD, and this reinforces the impression of a "liquid state." Furthermore, Fig. 3(d) compares the radial electron densities for the EXD, RVEM-diag, and

TABLE II. Participation weights (sum of coefficients squared) of different subspaces to the RVEM-diag wave function for $N = 6$ and $L = 47$. The total dimension of the RVEM-diag space considered is 78 (180 being the upper limit for the full TI subspace). The symbol $\Phi_{\mathcal{L}}^{\rm REM}(n_1,n_2)Q[\Lambda]$ ($L = \mathcal{L} + \Lambda$) denotes the subspace spanned by all the vibrations considered of the form $Q[\Lambda] \equiv Q_{\lambda_1}^{m_1} Q_{\lambda_2}^{m_2} Q_{\lambda_3}^{m_3}$ with $\Lambda = \lambda_1 m_1 + \lambda_2 m_2 + \lambda_3 m_3$.

RVEM subspace	Dimension	Weight
$\Phi_{45}^{\rm REM}(1,5)Q_2$	1	0.3549
$\Phi_{40}^{\rm REM}(1,5)Q[7]$	4	0.2283
$\Phi_{35}^{\rm REM}(1,5)Q[12]$	11	0.1485
$\Phi_{30}^{\rm REM}(1,5)Q[17]$	20	0.0400
$\Phi_{45}^{\rm REM}(0,6)Q_2$	1	0.1405
$\Phi_{39}^{\rm REM}(0,6)Q[8]$	8	0.0539
$\Phi_{33}^{\rm REM}(0,6)Q[14]$	22	0.0262
$\Phi_{47}^{\rm REM}(2,4)$	1	0.0002
$\Phi_{43}^{\rm REM}(2,4)Q[4]$	2	0.0012
$\Phi_{39}^{\rm REM}(2,4)Q[8]$	8	0.0059

Laughlin states. Again, the deviation between the EXD and RVEM-diag radial EDs is smaller than the deviation between the EXD and Laughlin radial EDs. This behavior is in agreement with the fact that the overlap between the EXD and RVEM-diag states is 0.990, while that between the EXD and the Laughlin state is smaller,[44,45] i.e., 0.982.

B. The case $N = 6$ with $L = 47$

For $N = 6$ and $L = 47$, the dimension of the EXD Hilbert space is 1540. The translationally invariant[20] (TI) subspace spanned by the RVEM wave functions has a much smaller dimension of 180. Here we analyze RVEM-diag results (see TABLE II) for a smaller RVEM basis of dimension 78; this suffices to yield a many-body yrast state having an 0.986 overlap with the EXD wave function and an energy relative error of 0.19% referenced to the EXD energy.

The state with $L = 47$ is not a cusp state [see Fig. 1(a)]. As a result the RVEM component with highest contribution is expected to have the form $\Phi_{45}^{\rm REM}(1,5)Q_2|0\rangle$, given that the (1,5) molecular configuration is predominant in the nearest $L = 45$ cusp state (see Fig. 2), and corresponding to the fact that two units of angular momentum separate 47 from 45. This expectation is confirmed by the RVEM-diag results in TABLE II, where the participation weight of this Q_2 component is listed to be 0.3549. We note that vibrations associated with the (1,5) isomer contribute the most with a (combined) participation weight of 0.7717, while those associated with the (0,6) isomer contribute only by 0.2206. The (2,4) isomer has a much smaller contribution with a weight of 0.0073.

Restating the above, we note that for $N = 6$ and $L = 47$ the vibrationless (1,5) component does not contribute to this LLL state. This is due to the fact that this state is

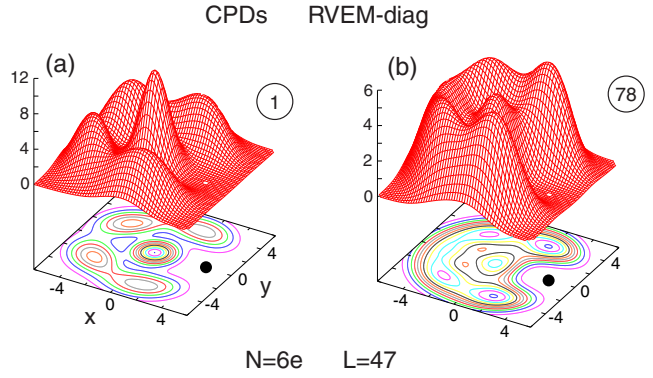

FIG. 4. (Color online) RVEM-diag CPDs for the non-cusp yrast state with $N = 6$ and $L = 47$. (a) Only one RVEM state [namely, $\Phi_{45}^{\rm REM}(1,5)Q_2$ with the largest participation, see TABLE II] is included in the RVEM basis. (b) The CPD corresponding to the largest number of RVEM states considered in TABLE II. The solid dots denote the position of the fixed point. The CPD in (b) exhibits only minor differences from the EXD-calculated CPD in Fig. 2(e). The circled numbers denote the number of states included in the RVEM expansion. The units for the vertical axes are arbitrary, but the same for all CPD frames here and throughout the paper. Lengths in units of l_B.

a non-cusp yrast state. The component with the largest participation weight is $\Phi_{45}^{\rm REM}(1,5)Q_2$; it corresponds to a dipolar ($\Lambda = 2$) vibration of the largest component [i.e., $\Phi_{45}^{\rm REM}(1,5)$] in the nearest cusp state with $L = 45$.

In Fig. 4, the CPD of the largest component of the RVEM-diag calculated for $L = 47$, that is $\Phi_{45}^{\rm REM}(1,5)Q_2$, is compared with the CPD associated with the the wave function resulting from the RVEM diagonalization for the maximum expansion (78 RVEM states) considered in TABLE II. While the effect of the dipolar Q_2 vibration in softening electron localization is visible when comparing to the pure REM CPD [compare Fig. 4(a) to Fig. 3(a)], the importance of the remaining additional vibrational modes in bringing a close agreement with the CPD obtained from the EXD calculation is apparent [compare Fig. 4(b) to the EXD-calculated CPD in Fig. 2(e)].

III. PINNED ELECTRON MOLECULE AND THE DESCRIPTION OF CRYSTAL-TYPE BEHAVIOR

The experimentally observed rf or microwave resonances in the spectrum of a 2D electon system under high B have been interpreted[8–10,18,19] as collective modes of a weakly pinned (due to disorder) Wigner-solid phase. Within the context of the LLL Hilbert space of a finite system, pinning can be described by a many-body Hamiltonian having the following two terms in addition to the Hamiltonian in Eq. (1): (i) impurity-type external potentials denoted by $V_{\rm imp}$ and (ii) an overall confinement Hamiltonian term denoted by $H_{\rm con}$. Namely,

$$\mathcal{H} = H_{\rm LLL}^{\rm int} + H_{\rm con} + V_{\rm imp}. \tag{10}$$

The confinement Hamiltonian accounts for the neutralizing ionic background,[28–33] and (for a smooth edge) it can be approximated as being harmonic

$$H_{\rm con} = \sum_{i=1}^{N} \frac{1}{2m^*}\left(\mathbf{p}_i - \frac{e}{c}\mathbf{A}_i\right)^2 + \sum_{i=1}^{N}\frac{1}{2}m^*\omega_0^2\mathbf{r}_i^2. \tag{11}$$

In Eq. (11), $\mathbf{p}$ is the momentum of an electron and $\mathbf{A}(\mathbf{r}) = (-By, Bx, 0)/2$ is the vector potential.

In the presence of the confinement, the degeneracy of the single-particle orbitals within each Landau level is lifted. In the high-magnetic field regime condidered in this paper ($\omega_0 << \omega_c$), the harmonic-confinement part involves only the Darwin-Fock levels that form the LLL band, and it can be approximated[26,27] simply as

$$H_{\rm LLL}^{\rm con} = \hbar(\sqrt{\omega_0^2 + \omega_c^2/4} - \omega_c/2)L. \tag{12}$$

Since $H_{\rm LLL}^{\rm con}$ is linear in the total angular momentum L, it influences only the total energies of the LLL states, but not their many-body structure [determined solely by $H_{\rm LLL}^{\rm int}$, see Eq. (1)]. We note that the description of pinning below is independent of the precise value of ω_0.

The first two terms in Eq. (10) define the "global" Hamiltonian

$$H_{\rm glb} = H_{\rm LLL}^{\rm int} + H_{\rm LLL}^{\rm con}, \tag{13}$$

which provides the global ground state of the system at a given B (in the absence of disorder).

An example of a global LLL spectrum (as a function of the applied magnetic field) corresponding to the Hamiltonian $H_{\rm glb}$ is displayed in Fig. 5. Specifically, for $N = 6$ electrons the global LLL spectrum is plotted in the neighborhood of $\nu = 1/3$ ($L = 45$). It is seen that only cusp states (see Fig. 1) become ground states [specifically for $L = 40$, 45, and 50, associated with the (1,5) molecular configuration]. The first excited states are separated from the ground states by relatively large energy gaps and are composed of these (1,5) cusp states and those associated with the (0,6) molecular configuration (with $L = 39$ and 51, see Fig. 1).[46] The remaining LLL states in Fig. 1, including the rest of the yrast states (e.g., with $L = 41$, 42, 43, 44, 46, 47, 48, 49) become higher excitations in Fig. 5.

The effect of the pinning perturbation term $V_{\rm imp}$ in Eq. (10) is to mix global states with good L and produce a wave packet without a good total angular momentum. For a weak pinning case (small perturbation $V_{\rm imp}$), it is apparent that $V_{\rm imp}$ can efficiently mix only two global ground states in the neighbohood of their crossing points (denoted by arrows in Fig. 5). Thus a weakly pinned state will have in general the form

$$\Phi^{\rm PIN}(L_1, L_2; \alpha, \beta) = \alpha\Phi_{L_1} + \beta e^{i\theta}\Phi_{L_2}, \tag{14}$$

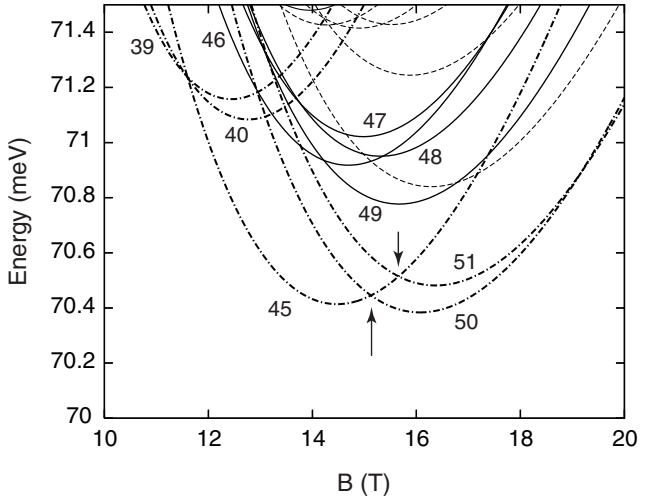

FIG. 5. The global spectrum as a function of the magnetic field in the neighborhood of $\nu = 1/3$ for $N = 6$ LLL electrons. The confinement was taken as $\hbar\omega_0 = 3.6$ meV. Note that all global ground states are yrast cusp states (see Fig. 1), but not all cusp states become global ground states.[22,26,27] The yrast cusp states with $L = 39$ (0,6), 40 (1,5), 45 (1,5), 50 (1,5), 51 (0,6) are portrayed by thick dashed-dotted lines. The $L = 45$ curve relates to $\nu = 1/3$ in the thermodynamic limit. The numbers next to some curves (for yrast states only) denote the corresponding total angular momenta. The arrows highlight a couple of curve crossings (for curves associated with cusp states). Remaining parameters: $\kappa = 13.1$ and $m^* = 0.067m_e$, corresponding to GaAs. The topology (relative position) of the curves is independent of the specific value for $\hbar\omega_0$ (see text).

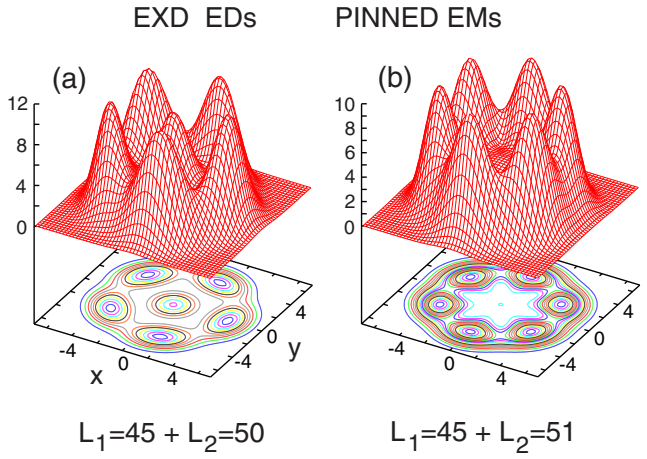

FIG. 6. (Color online) Electron densities for pinned [see Eq. (14)] LLL states in the neighborhood of $\nu = 1/3$ for $N = 6$ electrons. EXD states have been used for both Φ_{L_1} and Φ_{L_2}. (a) $L_1 = 45$ and $L_2 = 50$ ($|L_1 - L_2| = 5$). (b) $L_1 = 45$ and $L_2 = 51$ ($|L_1 - L_2| = 6$). The formation of a pinned (nonrotating) EM representing a (1,5) molecular configuration in (a) and a (0,6) molecular configuration in (b) is transparent. $\alpha = \beta = 1/\sqrt{2}$. Note that all six humps of localized electrons are visible in the electron densities of the pinned EM (in contrast to five visible humps in the CPDs of a rotating electron molecule). Lengths in units of l_B. The units of the vertical axes are $10^{-2}l_B^{-2}$. The electron densities are normalized to the number of particles, N.

where L_1 and L_2 are the magic angular momenta of the global ground states and $\alpha^2 + \beta^2 = 1$. The phase θ determines the orientation of the pinned state; we mention it here for the sake of generality and completeness, but it is not an essential parameter for the rest of the paper.

It is apparent that the total angular momentum of the wave packet state in Eq. (14) is not a good quantum number and is given as the average value

$$\bar{L} = \alpha^2 L_1 + \beta^2 L_2. \tag{15}$$

Likewise, the energy of the pinned state is given as the average of the energies E_1 and E_2 of the superimposed states

$$E^{\rm PIN}(L_1, L_2, \alpha, \beta) = \alpha^2 E_1 + \beta^2 E_2. \tag{16}$$

To demonstrate that weak pinning leads to formation of a nonrotating Wigner-crystal-type state, we display in Fig. 6 the electron densities for (a) $\Phi^{\rm PIN}(45, 50; 1/\sqrt{2}, 1/\sqrt{2})$ and (b) $\Phi^{\rm PIN}(45, 51; 1/\sqrt{2}, 1/\sqrt{2})$, where EXD yrast states have been used for both Φ_{L_1} and Φ_{L_2}. Fig. 6 demonstrates that the pinning of LLL states leads to formation of explicitly nonrotating EMs with the molecular configurations being present in the electron densities themselves. This amounts to a "reverse projection"[47] – that is, construction of a symmetry-broken, nonrotating, pinned state via superposition of symmetry-conserving, liquid-like states (with good total angular momenta), which themselves are characterized by azimuthally uniform electron densities [see Figs. 2(a-c)], but exhibit intrinsic crystalline correlations manifested in the corresponding CPDs [see Figs. 2(d-f)].

A remarkable trend revealed by the EDs in Fig. 6 is that the (1,5) molecular configuration corresponds to a superposition of two EXD yrast states with angular momenta differing by $|L_1 - L_2| = 5$ angular momentum units, while the (0,6) molecular configuration corresponds to a superposition of two EXD yrast states with angular momenta differing by $|L_1 - L_2| = 6$ units. This motivated us to study the ED patterns in the neighborhood of $\nu = 1/3$ for the superposition of two EXD yrast states as a function of the difference $\Delta L = |L_1 - L_2|$ (in particular for $\Delta L = 2, 3$ and 4; see Fig. 7). Of course the cases portrayed in Fig. 7 involve mixing with excited states, which are separated from the global ground state ($L_1 = 45$) by larger energy gaps (see Fig. 5) and are not expected to materialize in a weak-pinning situation. Fig. 7 illustrates that these combinations lead to formation of charge density waves (CDWs) instead of Wigner-molecular crystallites (as in Fig. 6). The relative amplitudes of the oscillations in the EDs shown in Figs. 7(a-c), referenced to the WM with $\Delta L = 5$ [Fig. 6(a)],

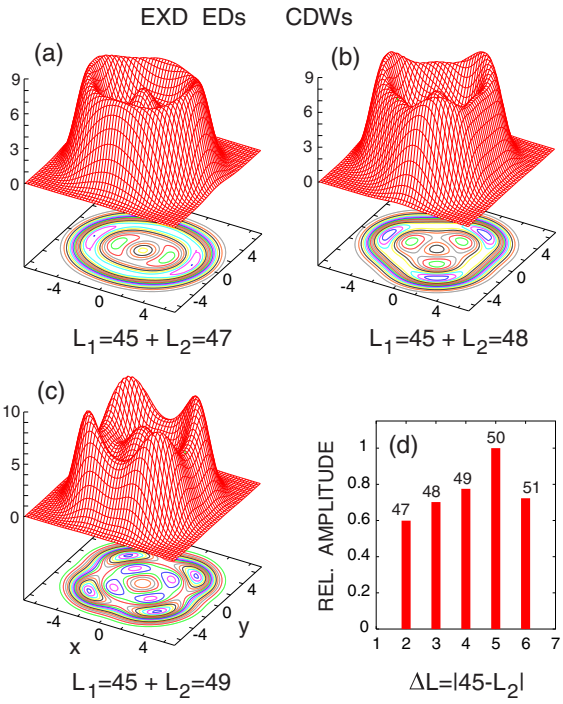

FIG. 7. (Color online) Electron densities corresponding to charge density waves for pinned [see Eq. (14)] LLL states in the neighborhood of $\nu = 1/3$ for $N = 6$ electrons (corresponding to angular momenta around $L = 45$). EXD states have been used for both Φ_{L_1} and Φ_{L_2}. (a) $L = 45$ and $L_1 = 47$ ($|L_1 - L_2| = 2$). (b) $L_1 = 45$ and $L_2 = 48$ ($|L_1 - L_2| = 3$). (c) $L_1 = 45$ and $L_2 = 49$ ($|L_1 - L_2| = 4$). Unlike the cases in Fig. 6, the EDs here are not commensurate with the (1,5) or (0,6) classical Wigner-molecule equilibrium configurations; instead they represent charge density waves. (d) The relative amplitude of the density oscillations as a function of $\Delta L = |45 - L_2|$, referenced to the WM case with $\Delta L = 5$ [which is the strongest one, see Fig. 6(a)]. The numbers above the vertical bars denote the values of L_2. Lengths in units of l_B. The units of the vertical axes are $10^{-2} l_B^{-2}$. The electron densities are normalized to the number of particles, N.

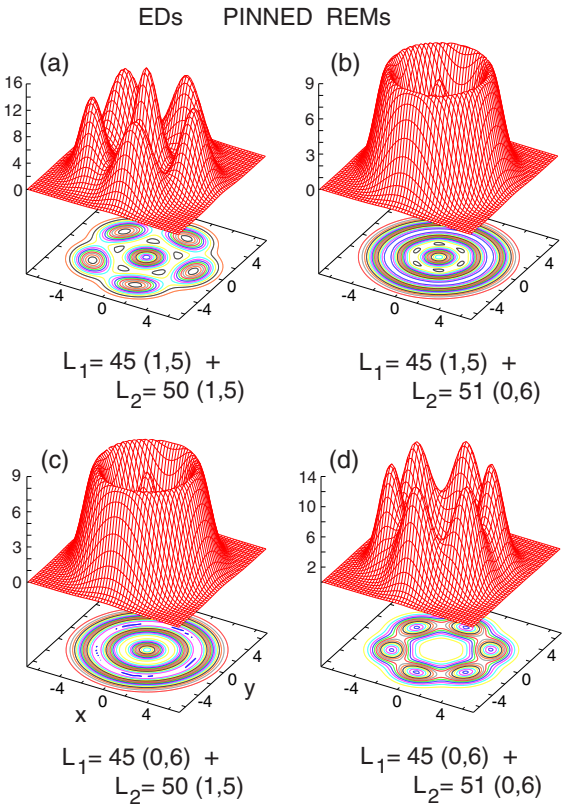

FIG. 8. (Color online) Electron densities for pinned [see Eq. (14)] LLL states in the neighborhood of $\nu = 1/3$ for $N = 6$ electrons. Pure REM states $\Phi_L^{\rm REM}(n_1, n_2)$ have been used for forming the superposition in Eq. (14). (a) $L_1 = 45$ and $L_2 = 50$; with a (1,5) molecular isomer. (b) $L_1 = 45$ (1,5) and $L_2 = 51$ (0,6). (c) $L_1 = 45$ (0,6) and $L_2 = 50$ (1,5). (d) $L_1 = 45$ and $L_2 = 51$; both with a (0,6) isomer. The formation of a pinned (static) Wigner molecule representing a (1,5) molecular configuration in (a) and a (0,6) molecular configuration in (d) is apparent. Superpositions of REM functions belonging to different isomers [(b) and (c)] fail to produce a pinned crystalline structure. $\alpha = \beta = 1/\sqrt{2}$. The units of the vertical axes are $10^{-2} l_B^{-2}$. The electron densities are normalized to the number of particles, N.

are shown in Fig. 7(d) exhibiting attenuated variations in the density.

Fig. 8 portrays the electron densities associated with superposition of pure REM wave functions $\Phi_L^{\rm REM}(1,5)$ and $\Phi_L^{\rm REM}(0,6)$ for $N = 6$ electrons. Such REM functions are the strongest components in the RVEM expansions of the EXD LLL states for $L = 45$, $L = 50$, and $L = 51$. We note that the magic angular momentum $L = 45$ is commensurate with both the (1,5) and (0,6) isomeric structures, while the magic $L = 50$ and $L = 51$ are commensurate only with one isomer, i.e., the (1,5) for the former and the (0,6) for the latter. Fig. 8 shows that superposition of same-configuration RVEM functions leads to pinned WMs [see Figs. 8(a) for (1,5) and 8(d) for (0,6)]. In contrast, superposition of RVEM functions corresponding to different isomers fails to generate any crystalline structures. This means that the emergence of the EXD pinned crystallites (such as in Fig. 6) cannot be explained (or anticipated) without the prior knowledge of the presence of appropriate $(n_1, n_2, ..., n_r)$ isomeric RVEM functions as physical components in the EXD LLL states with good L [see, e.g, the RVEM expansions in TABLE I and TABLE II, and in Ref. 20].

The above considerations culminate in the following "selection rules" for the construction of pinned Wigner-molecule crystallites: (I) The difference between the angular momenta of the superimposed states [e.g., L_1 and L_2 in Eq. (14)] should be a multiple of the magic angular momentum period associated with cusp states [e.g., either $\Delta L = 5$ or 6 for $N = 6$, see Fig. 1(a)]. (II) A given isomer [e.g., (1,5) or (0,6) for $N = 6$] must have a participation weight in both the symmetry-conserving superimposed states (for the participation weights for $N = 6$ and $L = 45$, see TABLE I). Naturally, different participa-

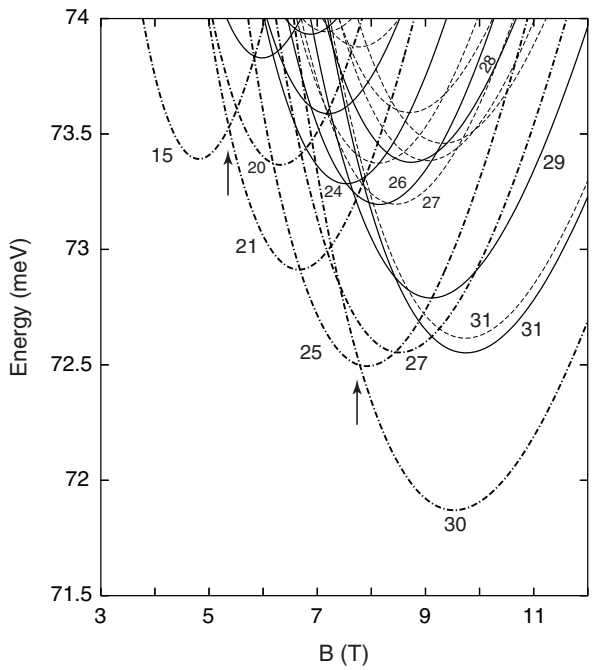

FIG. 9. The global spectrum as a function of the magnetic field in the neighborhood of $\nu = 1$ for $N = 6$ LLL electrons. The confinement was taken as $\hbar\omega_0 = 3.6$ meV. Note that all global ground states are yrast cusp states, but not all cusp states become global ground states.[22,26,27] The yrast cusp states with $L = 15$, 20 (1,5), 21 (0,6), 25 (1,5), 27 (0,6), 30 (1,5) are portrayed by thick dashed-dotted lines. The $L = 15$ curve relates to $\nu = 1$ in the thermodynamic limit. The numbers next to some curves denote the corresponding total angular momenta. Yrast states in addition to the cusp states are portrayed by a solid line. The arrows highlight a couple of curve crossings (for curves associated with cusp states). Remaining parameters: $\kappa = 13.1$ and $m^* = 0.067m_e$, corresponding to GaAs. The topology (relative position) of the curves is independent of the specific value for $\hbar\omega_0$ (see text).

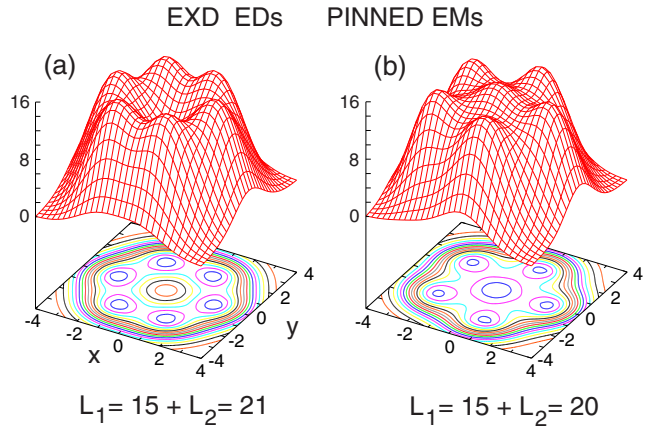

FIG. 10. (Color online) Electron densities for pinned [see Eq. (14)] LLL states in the neighborhood of $\nu = 1$ ($L = 15$) for $N = 6$ electrons. EXD states have been used for both Φ_{L_1} and Φ_{L_2}. (a) $L_1 = 15$ and $L_2 = 21$ ($|L_1 - L_2| = 6$). (b) $L_1 = 15$ and $L_2 = 20$ ($|L_1 - L_2| = 5$). The formation of a pinned (nonrotating) EM representing a (0,6) molecular configuration in (a) and a (1,5) molecular configuration in (b) is transparent. $\alpha = \beta = 1/\sqrt{2}$. Lengths in units of l_B. The units for the vertical axes are $10^{-2} l_B^{-2}$. The electron densities are normalized to the number of particles, N.

tion weights give rise to different strengths of the density oscillations in the Wigner-molecule crystallites [see Fig. 7(d)].

IV. PINNED ELECTRON MOLECULE IN THE NEIGHBORHOOD OF $\nu = 1$

The recent experimental observation in the neighborhood of $\nu = 1$ (in addition to the $\nu = 1/3$ neighborhood) of a microwave resonance in the spectrum of a 2D electon system under high B has also been associated with the formation of a weakly-pinned Wigner solid.[18,19] In this Section, following an analysis similar to that used in Sec. III for the $\nu = 1/3$ neighborhood, we show that crystallite states (precursors to a Wigner solid in the thermodynamic limit) develop also naturally for a finite system in the neighborhood of $\nu = 1$.

We start by displaying in Fig. 9 the global spectrum for $N = 6$ electrons; in this case $L = L_0 = 15$ corresponds to an integral filling factor $\nu = 1$ [see Eq. (2)]. The global LLL spectrum around $\nu = 1$ (Fig. 9) shares the same prominent characteristics with that in the neighborhood of $\nu = 1/3$ (Fig. 5), i.e., only yrast cusp states associated with magic angular momenta (here $L = 15$, 21, 25, 30) can become global ground states for a given magnetic field. The rest of the LLL states [derived from the interaction-only Hamiltoninan $H^{\rm int}_{\rm LLL}$; see Eq. (1)] become excited states in Fig. 9 and they are separated by substantial gaps from the global ground states.

As was pointed out in Sec. III, weak pinning results in the mixing of two global-ground states in the neighborhood of crossing points (see, e.g., arrows in Fig. 9), according to the prescription in Eq. (14). To demonstrate that weak pinning leads to formation of a nonrotating Wigner-crystal-type state in the neighborhood of $\nu = 1$, we display in Fig. 10 the electron densities for (a) $\Phi^{\rm PIN}(15, 21; 1/\sqrt{2}, 1/\sqrt{2})$ and (b) $\Phi^{\rm PIN}(15, 20; 1/\sqrt{2}, 1/\sqrt{2})$, where EXD yrast states have been used for both Φ_{L_1} and Φ_{L_2}. Fig. 10 shows that the pinning of LLL states in the neighborhood of $\nu = 1$ leads also to formation of explicitly nonrotating EMs, with the molecular configurations being present in the very electron densities. We stress again the property that a difference of $\Delta L = 6$ in angular momenta generates a (0,6) isomer, while a difference of $\Delta L = 5$ generates a (1,5) isomer; this was also the case in the neighborhood of $\nu = 1/3$ (see Fig. 6 and the selection rules given at the end of Sec. III).

We further note that the filling factor corresponding to the crossing point of the $L_1 = 15$ and $L_2 = 21$ global curves is 0.857, while the filling factor for the cross-

ing point of the $L_1 = 45$ and $L_2 = 50$ global curves is 0.316; here the filling factor is calculated from Eq. (2). As a result, we find that the pinned Wigner crystallite can appear in a larger range of filling factors away from $\nu = 1$ (i.e., $\Delta\nu = 0.143$) compared to the corresponding range in the neighborhood of $\nu = 1/3$ (where $\Delta\nu = 0.333 - 0.316 = 0.017$). This trend is in agreement with experimental observations.[18]

V. LARGER SIZES

In the previous sections, we addressed the interplay of liquid and crystalline states by studying in detail EXD results for the case of $N = 6$ electrons. Our findings, however, are not limited to the case of $N = 6$ electrons, but extend to larger sizes; this is supported by the EXD results presented in this section for sizes in the range from $N = 7$ to $N = 29$ electrons.

A. Extrapolation of total energies

In Fig. 11(a), we plot the three lowest global ground-state energies around $\nu = 1/3$ (for $N = 7$ electrons) as a function of the magnetic field B. They correspond to three cusp states with angular momenta 57, 63, and 69. The magnetic field corresponding to $\nu = 1/3$ is denoted by $B_{1/3}$, while those associated with the two crossing points A and C (left and right of $B_{1/3}$) are denoted as B_- and B_+, respectively. The AD dashed line corresponds to the broken-symmetry (pinned) Wigner-crystallite state $\Phi^{\rm PIN}(57, 63; 1/\sqrt{2}, 1/\sqrt{2})$ with energy $E^{\rm PIN} = E_{\rm glb}(L_1 = 57)/2 + E_{\rm glb}(L_2 = 63)/2$, while the EC dashed line corresponds to a pinned crystalline state $\Phi^{\rm PIN}(63, 69; 1/\sqrt{2}, 1/\sqrt{2})$ with energy $E^{\rm PIN} = E_{\rm glb}(L_1 = 63)/2 + E_{\rm glb}(L_2 = 69)/2$.

The energy cost (energy gap to be overcome) for mixing the $L = 63$ ground state at $\nu = 1/3$ with the excited state $L = 57$ directly (vertically) above it, yielding the pinned crystallite $\Phi^{\rm PIN}(57, 63; 1/\sqrt{2}, 1/\sqrt{2})$ is denoted by $\Delta_{\rm xc}$ [see Fig. 11(a)]. Most importantly, at B_- (or B_+) the good-angular momentum states $L_1 = 57$ and $L_2 = 63$ (or $L_1 = 63$ and $L_2 = 69$) are degenerate and thus the energy cost (gap) for creating the crystallite from a superposition of two angular momenta states vanishes. The least favorable place (that is, the largest energy cost) for creating the crystallite is at $B_{1/3}$, while, as aforementioned, at $B_-(B_+)$ the cost vanishes. Since $\nu_{1/3}B_{1/3} = \nu_-B_- = \nu_+B_+$ (keeping the electron density constant), this correlates with the experimentally observed continuous reduction of the microwave absorption strength as the filling factor ν approaches the value 1/3, reflecting the enhanced stability of the liquid state at $\nu = 1/3$ compared to the crystalline one. As one moves away from $B_{1/3}$, the energy cost for creating the crystallite decreases, so that a weaker disorder can act as a pinning perturbation leading to the formation of the crystallite, as illustrated in Fig. 11.

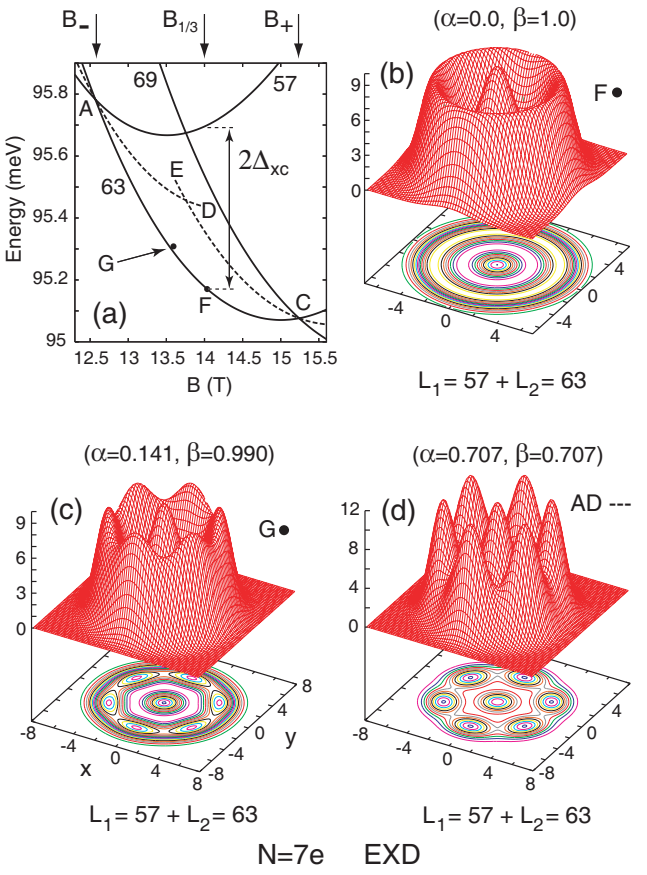

FIG. 11. (Color online) (a) The global energy spectrum [ground state ($L = 63$) and first excited states ($L = 57$ and $L = 69$)] at $\nu = 1/3$ (and its neighborhood) for $N = 7$ electrons, as a function of the magnetic field B. The magnetic field corresponding to filling factor $\nu = 1/3$ is denoted by $B_{1/3}$, and those corresponding to the crossing points A and C are denoted by B_- and B_+. The dashed lines indicate the energies for the pinned crystalline states [Eq. (14)] $\Phi^{\rm PIN}(57, 63; 1/\sqrt{2}, 1/\sqrt{2})$ (AD, left dashed line) and $\Phi^{\rm PIN}(63, 69; 1/\sqrt{2}, 1/\sqrt{2})$ (EC, right dashed line). (b-d) These panels portray the elecrton density of the pinned crystallite $\Phi^{\rm PIN}(57, 63; \alpha, \beta)$ for various values of the weights α and β, corresponding to different degrees of pinning at the points marked in (a) as F and G and on the dashed-line segment marked in (a) as AD. In (a) the points marked F, G and A can be reached via a weak-pinning disorder, while moving from A to D along the dashed line would require strong-pinning disorder. The energy cost (gap) for mixing the ground state ($L = 63$) with the first excited state ($L = 57$) at $B_{1/3}$ [point marked F in (a)] is denoted as $\Delta_{\rm xc}$. The confinement was taken as $\hbar\omega_0 = 3.6$ meV. Remaining parameters: $\kappa = 13.1$ and $m^* = 0.067m_e$, corresponding to GaAs. The topology (relative position) of the curves is independent of the specific value for $\hbar\omega_0$ (see Sec. III). Lengths in units of l_B. The units of the vertical axes are $10^{-2}l_B^{-2}$. The electron density is normalized to the number of particles, N.

The gradual development of a Wigner crystallite in

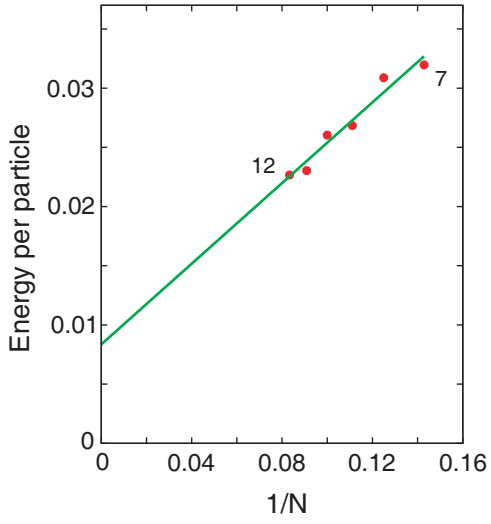

FIG. 12. (Color online) Extrapolation of the EXD-calculated [see Eq. (1)] energy gap per particle, $2\Delta_{\rm xc}/N$, at $\nu = 1/3$ to the thermodynamic limit ($1/N \to 0$). Results are shown in the range $N = 7$ to $N = 12$ (see TABLE III). In the thermodynamic limit, the energy cost per particle, $\Delta_{\rm xc}/N$, to create a pinned crystal at precisely $\nu = 1/3$ is approximately $0.004e^2/\kappa l_B$. Vertical axis: Energies per particle in units of $e^2/\kappa l_B$. Horizontal axis: $1/N$ where N is the number of electrons.

the neighborhood of 1/3 for weak-pinning conditions is illustrated in Fig. 11(b-d), where the pinned state is illustrated at the points marked F, G, and A, respectively. To simulate the experimental finding of a liquid state at $\nu = 1/3$ ($B_{1/3}$), we assume a sufficiently weak pinning so that the weights α and β in the superposition $\alpha\Phi_{L_1=57} + \beta\Phi_{L_2=63}$ [see Eq. (14)] can be taken as $\alpha = 0$ and $\beta = 1$; indeed the electon density in Fig. 11(b) is circularly symmetric corresponding to a liquid state. We remark that because of the large mixing energy gap at $B_{1/3}$, creation of a pinned crystalline state at $\nu = 1/3$ requires strong-pinning disorder. The electron density associated with a pinned crystallite shown in Fig. 11(c) [corresponding to the point marked G in Fig. 11(a)] was obtained via weak-pinning induced mixing ($\alpha = 0.141, \beta = 0.990$). This electron density exhibits partially developed crystalline features, with a (1,6) electronic configuration. A fully developed (1,6) crystallite (obtained for $\alpha = \beta = 1/\sqrt{2}$) is shown in Fig. 11(d) [corresponding to the point marked as A in Fig. 11(a)], which as aforementioned is associated with a vanishing mixing gap (i.e., most susceptible to pinning by weak disorder).

To gain further insights into the nature of the Wigner crystalline states considered in this paper, it is instructive to extrapolate the EXD-calculated $\Delta_{\rm xc}$ as a function of $1/N$ (where N is the number of electrons) to the thermodynamic limit (i.e., $1/N \to 0$). Such extrapolation (see Fig. 12 and TABLE III) allows us to compare our results with previous treatments of the Wigner crystal based on variational wave functions in the bulk;[4,6,14] the latter results are summarized in TABLE IV. Since the results from the bulk wave functions[4,6,14] assume that the kinetic energy of all the electrons is quenched to the value of the LLL energy, $\hbar\omega_c$,[30,33] we need to omit kinetic energy contibutions from $\Delta_{\rm xc}$ when making comparisons; the energies used in Fig. 12 correspond to spectra like the one shown for $N = 6$ in Fig. 1. Then $2\Delta_{\rm xc}$ is given by the difference $|E_1^{\rm int} - E_2^{\rm int}|$ of the electron-electron interaction energies [the eigenenergies of the Hamiltonian in Eq. (1)] associated with the yrast state with (magic) angular momentum $L = 3L_0 = 3N(N-1)/2$ ($\nu = 1/3$) and the (magic) yrast state immediately preceeding it; see detailed description in TABLE III.

Inspection of the values in TABLE IV leads us to conclude that the Wigner crystalline state described by our treatment entails the smaller gap (energy cost) of the crystal relative to the liquid state at $\nu = 1/3$, compared to previous treatments. This finding is a consequence of the *quantum* nature of our crystalline state, exhibiting a high degree of electronic correlations. Since $\Delta_{\rm xc}$ is largest at $\nu = 1/3$ [see Fig. 11(a)], the above conclusion extends to the crystalline states formed (via weak-disorder pinning) in the whole neighborhood of $\nu = 1/3$.

B. Evolution of crystalline patterns

In this section, we discuss the evolution of the pinned EXD crystalline patterns as a function of size (the number of electrons N). In Fig. 11, in addition to the $N = 6$ system discussed in detail in earlier sections, we presented results for pinned Wigner crystallites in the neighborhood of $\nu = 1/3$ for $N = 7$ electrons; they conform to a (1,6) molecular configuration in agreement with the finite-size crystalline structures for repelling classical point charges.[38,39]

Currently, for $N > 10$, it is not computationally convenient to calculate electron densities (or CPDS) in the neighborhood of $\nu = 1/3$. However, given the fact that the crystalline isomeric structures are independent of the filling factor ν (they depend only on the number of electrons N; compare Sec. III and Sec. IV), we can use EXD results in the neighborhood of $\nu = 1$ to study the evolution of pinned crystallites with size, without loss of

TABLE III. Interaction energies per particle [see the Hamiltonian in Eq. (1)] from $N = 7$ to $N = 12$ of the yrast states entering in the evaluation of the gap $2\Delta_{\rm xc}/N$. (n_1, n_2) denotes the ring configuration. Energies in units of $e^2/\kappa l_B$.

N	(n_1, n_2)	L_1	L_2 ($3L_0$)	$E_1^{\rm int}/N$	$E_2^{\rm int}/N$
7	(1,6)	57	63	0.57409	0.54213
8	(1,7)	77	84	0.63462	0.60373
9	(2,7)	101	108	0.68860	0.66177
10	(2,8)	127	135	0.74287	0.71684
11	(3,8)	157	165	0.79218	0.76915
12	(3,9)	189	198	0.84187	0.81921

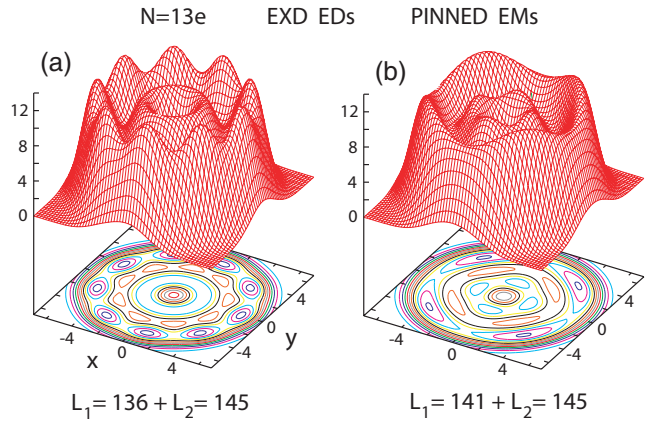

FIG. 13. (Color online) Electron densities for pinned (crystalline) [see Eq. (14)] LLL states in the neighborhood of $\nu = 1$ for $N = 13$ electrons. (a,b) Formation of a pinned (nonrotating) EM representing a (4,9) molecular configuration is evident. In (a) $L_2 - L_1 = 9$, with the outer ring showing nine density humps, and in (b) $L_2 - L_1 = 4$, showing four density peaks on the inner ring. $\alpha = \beta = 1/\sqrt{2}$. Lengths in units of l_B. The units of the vertical axes are $10^{-2} l_B^{-2}$. The electron density is normalized to the number of particles, N.

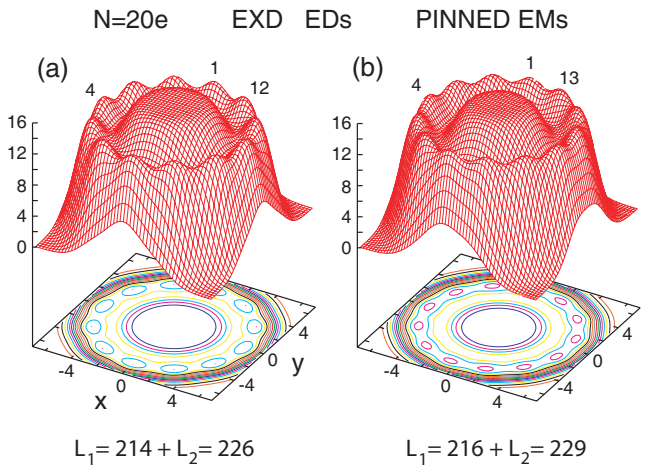

FIG. 14. (Color online) Electron densities for pinned [see Eq. (14)] LLL states in the neighborhood of $\nu = 1$ for $N = 20$ electrons. In (a) $L_2 - L_1 = 12$ corresponding to twelve electrons on the outer ring, and in (b) $L_2 - L_1 = 13$, with thirteen electrons on the outer ring. These electron densities correspond to formation of pinned (nonrotating) EM isomers representing a (1,7,12) molecular configuration (a) and a (1,6,13) molecular configuration (b). $\alpha = \beta = 1/\sqrt{2}$. Lengths in units of l_B. The units of the vertical axes are $10^{-2} l_B^{-2}$. The electron density is normalized to the number of particles, N.

generality.

To this end, we present EXD calculated electron densities of pinned crystallites for three (larger than $N = 6$) sizes, i.e., $N = 13$ (Fig. 13), $N = 20$ (Fig. 14), and $N = 29$ (Fig. 15).

In accordance with the selection rules described in Sec. III, the pinned EM for $N = 13$ resulting from mixing states with $L_1 = 136$ and $L_2 = 145$ exhibits a 9-electron outer ring ($L_2 - L_1 = 9$) [Fig. 13(a)], and the one with $L_1 = 141$ and $L_2 = 145$ shows a 4-electron inner ring ($L_2 - L_1 = 4$) [Fig. 13(b)]. The superposition of these two mixed states gives the (4,9) pinned configuration. For $N = 20$ (Fig. 14) and $N = 29$ (Fig. 15), we focus on the electron configurations in the outer rings of the pinned EM crystallites; the classical molecular isomers[38,39] exhibit the (1,7,12) and (1,6,13) crystalline configurations for $N = 20$ and the (4,10,15) and (5,10,14) configurations for $N = 29$. It is evident that the quantum mechanical Wigner configurations of the outer rings in the EXD-calculated EDs in Fig. 14 and Fig. 15 are in agreement with the above classical patterns. For these sizes, i.e., $N = 20$ and $N = 29$, exploration of the molecular configurations of the electrons in the inner rings via EXD calculations will require consideration of higher angular momenta and a heavier computational effort, beyond the scope of this paper.

To summarize: For all sizes (in the range of $N = 6$ to $N = 29$) that we considered here (and for angular momentum values that we have been able to reach, at the present time, via quantum mechanical EXD calculations), the pinned crystalline configurations characterizing the electron densities are in agreement with those obtained from structural optimization of Coulomb repelling classical point charges confined by a 2D circular harmonic potential.[38,39] This finding is particularly noteworthy since the LLL EXD wave functions are determined solely by the interelectron repulsion [see the Hamiltonian in Eq. (1)]. As discussed in the context of the classical calculations (see TABLE I in Ref. 38), these configurations develop gradually a core that possess a hexagonal Wigner-lattice structure for larger clusters (above hundred particles). The aforementioned agreement supports the conjecture that the quantum mechanical crystalline configurations described in this paper may be considered as embryonic Wigner crystallites extrapolating to the Wigner haxagonal lattice at the thermodynamic limit.

TABLE IV. Energy cost per particle at the thermodynamic limit (compared to the liquid state) for forming a Wigner-crystalline state at $\nu = 1/3$ according to previous approaches and the present work. Note that smaller values reflect higher stability of the crystal. Values corresponding to previous Wigner-crystal approaches were extracted from Fig. 2 in Ref. 14. Energies in units of $e^2/\kappa l_B$.

Approach	Energy cost per particle
Maki-Zotos[a] (Hartree Fock)	0.0245
Lam-Girvin[b]	0.0183
Yi-Fertig[c] (composite-fermion WC)	0.0070
Present Work[d]	0.0040

[a] Ref. 4
[b] Ref. 6
[c] Ref. 14
[d] see Fig. 12

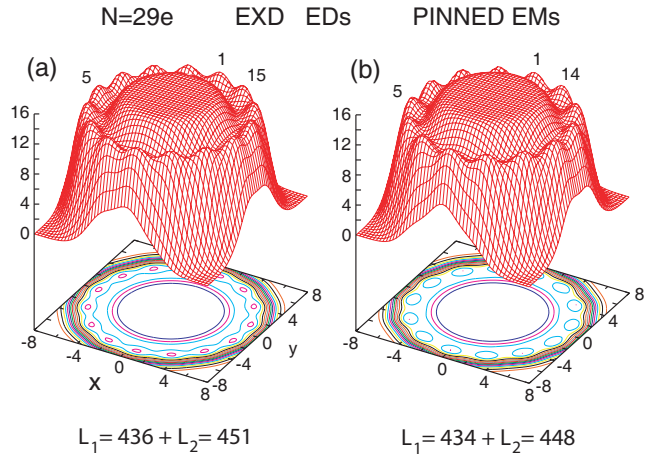

FIG. 15. (Color online) Electron densities for pinned (crystalline) [see Eq. (14)] LLL states in the neighborhood of $\nu = 1$ for $N = 29$ electrons. In (a) $L_2 - L_1 = 15$ corresponding to fifteen electrons on the outer ring, and in (b) $L_2 - L_1 = 14$, with fourteen electrons on the outer ring. These electron densities correspond to formation of pinned (nonrotating) EM isomers representing a (4,10,15) molecular configuration (a) and a (5,10,14) molecular configuration (b). $\alpha = \beta = 1/\sqrt{2}$. Lengths in units of l_B. The units of the vertical axes are $10^{-2} l_B^{-2}$. The electron density is normalized to the number of particles, N.

VI. DISCUSSION: COMPOSITE-FERMION-CRYSTAL APPROACHES VERSUS THE WIGNER SOLID IN THE NEIGHBORHOOD OF $\nu = 1/3$

The concept of a composite-fermion Wigner crystal was described[14] through the use of the wave function approach, i.e., by attaching Jastrow vortices (factors) to the Maki-Zotos[4] Hartree-Fock-crystal wave function. Of relevance for our purposes here is Fig. 2 in Ref. 14, where the energies of the CFWC are compared to those of the Laughlin liquid states[2] in the range $0.10 \leq \nu \leq 0.35$ (which includes the FQHE fillings 1/7, 1/5, and 1/3). From this figure,[14] it is evident that the CFWC energy lies far above the Laughlin-liquid energy in the neighborhood of $\nu = 1/3$. On the other hand the CFWC energy is competitive with the Laughlin energy in the neighborhood of $\nu = 1/5$, and it becomes lower than the Laughlin energy in the neighborhood of $\nu = 1/7$. The above trends suggest that the CFWC wave function is a legitimate candidate for the case of the Wigner solid in the neighborhood of $\nu = 1/5$, but *not* for the Wigner solid recently observed[18] in the neighborhood of $\nu = 1/3$. This is consistent with most of the subsequent studies[16,17] associated, or related, to CF crystals; indeed, we are unaware of any CF crystal study that addressed the neighborhood of $\nu = 1/3$.

The similarity between the IQHE and the FQHE was used in Ref. 48 to study whether the reentrant IQHE behavior[49] may occur also for CFs in higher CF Landau levels. According to this analogy, residual interactions between CF quasiparticles (that is excitations of the CF fractional quantum Hall effect liquid) may lead to formation of CF-solid phases, or to second-generation CF liquids. Ref. 48 employed the same Hamiltonian composite-fermion approach as Narevich *al.*[15] to model the CF solid and CF liquid phases around the electronic fractional fillings 4/11, 6/17, and 4/19, which are higher than 1/3. Such an approach (employing a two-component picture, i.e., CF liquid and its excitations), which has been noted in Ref. 18, contrasts with our approach where a single class of wave functions is used for both the liquid and Wigner-solid states.

Of relevance to our paper here is the fact that Ref. 48 did not produce new CF results in the neighborhood of $\nu = 1/3$ with respect to the previous composite-fermion Wigner-crystal studies[14] of Yi and Fertig. Furthermore the Hamiltonian CF approach employed in Ref. 48 appears not to describe the neighborhood of $\nu = 1/3$, since it is a weak-coupling perturbative method applicable[50] only to cases "when a higher CF LL level ($p \geq 1$) is *partially* filled"; it fails when the composite-fermion filling factor ($\nu_{\rm CF}$) is close to an integer value (corresponding to a closed CF shell). Note that for an electronic filling factor $\nu \sim 1/3$, one has $\nu_{\rm CF} \sim 1$.

The above approaches were explicitly based on a bulk 2D system. However, the liquid-like composite-fermion trial functions were formulated[11,13] in the context of a finite system. This offered several advantages, an important one being the ability to perform quantitative comparisons[13] with exact results (e.g., for energies) and wave functions (e.g., pair correlations and overlaps). The composite-fermion crystal in Refs. 16 and 17 (henceforth referred to as CFC, to distinguish it from the aforementioned infinite CFWC) represents an attempt to formulate a CF crystal for a finite system. The important new element in the CFC approach is the use of the correlated rotating-electron-molecule[21,23] wave function in the place of the *uncorrelated* single Slater determinant employed in the CFWC of Ref. 14. This substitution is nontrivial, and (in the framework of the CFC theory) it leads to restoration of the fundamental symmetries of the many-body Hamiltonian (rotational and translational) and to the introduction of additional energy-lowering correlations; a direct consequence is that the CFC wave function can be be tested against exact diagonalization calculations, due to the fact that it has a good total angular momentum, $L_{\rm CFC}$.

Because of its use of the REM (which is nonvanishing only for magic angular momenta, L_m), the CFC is limited solely to the FQHE filings, and cannot provide descriptions in the neighborhood of fractional fillings. Furthermore, a serious shortcoming of the CFC is its inability (by construction) to be extended to $\nu = 1/3$. Indeed the

angular momentum, $L_{\rm CFC}$, of the CFC is given by[16,17]

$$L_{\rm CFC} = N(N-1)p + L_{\rm REM}, \tag{17}$$

where the first term on the right-hand side is $2L_0p$, p is a nonnegative integer, and $L_{\rm REM}$ is the REM angular momentum. At $\nu = 1/3$, one needs to have $L_{\rm CFC} = 3L_0$, with L_0 [see Eq. (3)] being the lowest angular momentum. Then the only possible value for $L_{\rm REM}$ is L_0 ($p = 1$). The REM, however, at $L_{\rm REM} = L_0$ coincides[23] with the single Slater determinant of the maximun density droplet, and the usual attachment of two CF vortices to this determinant yields[11] the liquid Laughlin wave function for $\nu = 1/3$.

From the above discussion, it follows that the emergence of a Wigner solid in the neighborhood of $\nu = 1/3$ has been a challenging open problem in the composite-fermion literature up to date. Based on the insights gained in this paper and the equivalence[20] between the composite-fermion and the RVEM theories, we show (see Appendix B) that CF wave functions can be used to describe formation of Wigner crystallites through the pinning process introduced in Sec. III.

VII. SUMMARY

Based on the rotating-and-vibrating electron-molecule theory[20,21] (RVEM), and in conjunction with exact-diagonalization results, we presented a unified microscopic theory for the interplay between liquid and Wigner-solid states in the neighborhood of $\nu = 1/3$, which was recently observed[18] experimentally. In the RVEM theory, the description of both liquid and Wigner-solid states is achieved within the framework of a single class of variational wave functions; see Eqs. (5 and (6) and Refs. 20 and 21.

In the RVEM method, liquid characteristics of the FQHE states are associated with conservation of the symmetries of the Hamiltonian, in particular the total angular momentum of the RVEM wave functions. For example, the electron densities of the RVEMs are circularly symmetric as expected for liquid states [this is also in accordance with EXD results for all states of the LLL spectra, as illustrated for $N = 6$ electrons in the neighborhood of $\nu = 1/3$ in Fig. 2(a-c)]. The liquid characteristics of the LLL states, however, coexist with intrinsic correlations that are crystalline in nature [i.e., exhibit patterns associated with the equilibrium configurations of N classical point-like electrons, as revealed via the conditional probability distributions; see examples in Fig. 2(d-f)]. Further insight into the intrinsic crystalline correlations was gained via a study of the relative weights of the ro-vibrational excitations of the electron crystallite. For $N = 6$ electrons, examples of such relative weights were presented for states in the neighborhood of $\nu = 1/3$ in Secs. II A and II B.

Although the electron densities of the symmetry-conserving LLL states do not exhibit crystalline patterns, the intrinsic crystalline correlations are reflected in the emergence in the LLL spectra of cusp yrast states with enhanced stability and magic angular momenta (see Fig. 1); the cusp states are associated with the fractional fillings in the thermodynamic limit [see Eq. (2)]. A direct consequence of the enhanced stability is the fact that only states with magic angular momenta (cusp states) can become global ground states, as illustrated in Figs. 5 and 9 for $N = 6$ electrons and $\nu = 1/3$ and $\nu = 1$, respectively.

Away from the exact fractional fillings, weak pinning perturbations (experimentally due to weak disorder) can overcome the energy gaps between adjacent global states (in particular near their crossing points; see Fig. 5 and Sec. V) and generate a mixed, *broken symmetry* (pinned) ground state, that is a linear superposition of symmetry-conserving LLL states with different total angular momenta. A central finding of this paper is that such pinned states do exhibit explicitly a crystalline pattern in the electron density (nonrotating, pinned molecular, or Wigner, crystallites); see, e.g., Figs. 6 and 8). These pinned crystallites represent finite-size precursors of the Wigner solid in the thermodynamic limit (see Sec. V). Furthermore, we illustrated that the emergence of the pinned molecular crystallite is a direct consequence of the contributions of RVEM components in the symmetry-conserving LLL states themselves; see discussion in text related to Fig. 8.

Along with the molecular crystallites (see Figs. 6 and 8), other charge-density-wave patterns may develop, originating from the absence of certain commensurability conditions between the angular momentum states that get coupled in the pinning process (see Fig. 7). However, they correspond to coupling of the global ground states with excited global states, and therefore are less likely to materialize for a case of weak pinning, because of the large energy gaps between these states. Selection rules governing the formation of pinned Wigner crystallites were formulated at the end of Sec. III.

In addition to the neighborhood of $\nu = 1/3$, we also demonstrated that the RVEM approach can account in a similar unified manner for the interplay between liquid and Wigner solid states in the neighborhood of $\nu = 1$; see Sec. IV.

We note again here that our findings are not limited to the case of $N = 6$ electrons only. In Sec. V, exact-diagonalization results were presented in a wide range of sizes, from $N = 7$ to $N = 29$ electrons. The extrapolation displayed in Fig. 12 gave a value for the energy gap representing the stability of the bulk Wigner crystal. This value was compared to previously calculated estimates by other methods in TABLE IV; it was found to reflect a Wigner crystal of higher stability due to a large degree of quantum correlations. Furthermore, we showed in Sec. V that the pinned crystalline patterns obtained via our quantum mechanical calculations evolve (for all sizes considered in this paper, i.e., from $N = 6$ to $N = 29$ electrons) according to the well established sequence of configurations found for classical point charges, leading

to formation of Wigner-crystalline hexagonal cores for $N > 100$ electrons.

As aforementioned, the RVEM theory described here and applied to the analysis of the appearance of Wigner crystalline patterns in the neighborhood of $\nu = 1/3$ employs a single class of variational wave functions for the description of both the correlated liquid and Wigner-solid states. This theory differs in an essential manner from composite-fermion approaches[13] (including Laughlin's original formulation[2]) which utilize different classes of variational wave functions for representing the liquid versus Wigner-solid states. Specifically, in the CF approaches, FQHE states are associated with CF liquid states (defined in the context of N LLL electrons and preserving the total angular momentum[11,13]), while solid states are described by CF Wigner crystals;[14] the latter violate the conservation of the total angular momentum (broken symmetry) and are a modification (the attachment of Jastrow factors) of the Maki-Zotos[4] Wigner crystal for an infinite 2D system (defined on a triangular lattice at the mean-field Hartree-Fock level).[51]

In Sec. VI, we discussed the open challenges faced by the composite-fermion literature[13–17,48] in addressing the emergence of the Wigner-solid state in the neighborhood of $\nu = 1/3$. Based on the insights gained in this paper and the equivalence[20] between the composite-fermion and the RVEM theories, we show (see Appendix B) that CF wave functions can be used to describe formation of Wigner crystallites through the pinning process introduced in Sec. III.

The physical picture and formalism developed in this paper is expected to apply to other filling fractions. While future experimental and theoretical studies will be needed, our work suggests that liquid-Wigner-solid coexistence may occur for fractions in the neighborhood of which a Wigner crystal has not been seen as yet. Investigations of these issues with a variable (tunable) degree of disorder would be most valuable.

ACKNOWLEDGMENTS

This work was supported by the Office of Basic Energy Sciences of the US D.O.E. under contract FG05-86ER45234.

Appendix A: Purely rotational trial wave functions (REMs)

In this Appendix, we recapitulate the analytic formulas for the vibrationless REM trial wave functions entering into the general expression for the RVEM functions [see Eq. (5)]. The REM expresions for any $(n_1, n_2, \ldots, n_r)$ multi-ring configuration (with the number of electrons $N = \sum_{q=1}^{r} n_q$, n_q being the number of electrons in the qth ring) were derived earlier in Refs. 20–22.

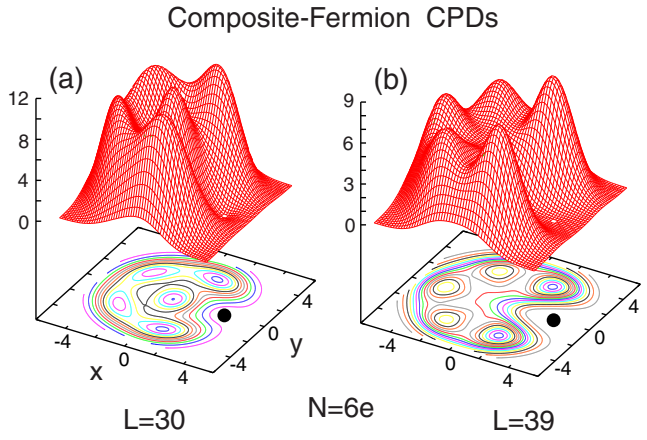

FIG. 16. (Color online) Composite-fermion CPDs for the cusp yrast states for $N = 6$ LLL electrons with (a) $L = 30$ ($\nu = 1/2$) and (b) $L = 39$. The compact CF trial functions for these L's were calculated for a disk geometry according to Sec. 4.3 of Ref. 53. The solid dots denote the position of the fixed point. The units for the vertical axes are arbitrary, but the same for all frames portraying CPDs throughout the paper. Lengths in units of l_B. Note the (1,5) and (0,6) molecular patterns for $L = 30$ (a) and $L = 39$ (b), respectively.

Assuming that $\mathcal{L}_1$ and $\mathcal{L}_2$ are the *partial* angular momenta for each ring ($\mathcal{L}_1 + \mathcal{L}_2 = \mathcal{L}$), the final two-ring (n_1, n_2) REM expression is

$$\Phi^{\rm REM}_{\mathcal{L}}(n_1, n_2)[z] = \sum_{\substack{l_1+l_2+\ldots+l_{n_1}=\mathcal{L}_1, l_{n_1+1}+l_{n_1+2}+\ldots+l_N=\mathcal{L}_2 \\ 0\le l_1<l_2<\ldots<l_{n_1}<l_{n_1+1}<\ldots<l_N}} C(l_1, l_2, \ldots, l_{n_1}) \times C(l_{n_1+1}, l_{n_1+2}, \ldots, l_N) \det[z_1^{l_1}, z_2^{l_2}, \ldots, z_N^{l_N}], \quad \text{(A1)}$$

where the z_i's are complex-number particle coordinates and "det" denotes a Slater determinant. The coefficients $C(l_1, l_2, \ldots, l_{n_1})$ and $C(l_{n_1+1}, l_{n_1+2}, \ldots, l_N)$ are calculated by applying to each one of them the single-ring $[(0, N)]$ expression

$$C(l_1, l_2, \ldots, l_N) = \left(\prod_{i=1}^{N} l_i!\right)^{-1} \left(\prod_{1\le i<j\le N} \sin\left[\frac{\pi}{N}(l_i - l_j)\right]\right). \quad \text{(A2)}$$

It is straighforward to generalize the two-ring REM expression in Eq. (A1) to more complicated or simpler [i.e., $(0, N)$ and $(1, N-1)$] configurations by (I) considering a separate factor $C(l_{n_{q-1}+1}, l_{n_{q-1}+2}, \ldots, l_{n_{q-1}+n_q})$ for each qth ring; (II) restricting the summation of the associated n_q angular momenta, i.e., $l_{n_{q-1}+1} + l_{n_{q-1}+2} + \ldots + l_{n_{q-1}+n_q} = \mathcal{L}_q$, with $\sum_{q=1}^{r} \mathcal{L}_q = \mathcal{L}$.

The analytic expressions for $\Phi^{\rm REM}_{\mathcal{L}}(n_1, n_2, \ldots, n_r)[z]$ describe pure molecular rotations associated with magic angular momenta

$$\mathcal{L} = L_m \equiv L_0 + \sum_{q=1}^{r} n_q k_q, \quad \text{(A3)}$$

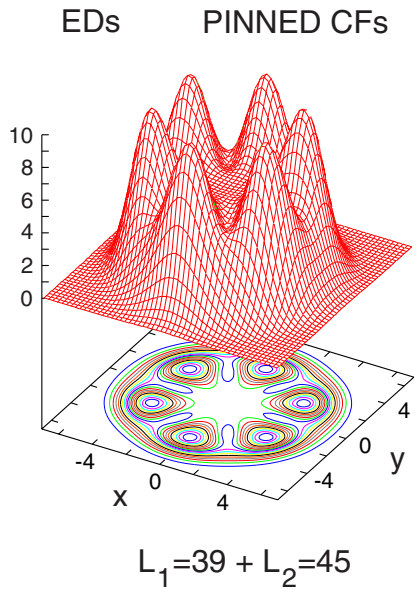

FIG. 17. (Color online) Electron densities for pinned [see Eq. (14)] LLL states in the neighborhood of $\nu = 1/3$ for $N = 6$ electrons. Compact CF states have been used for both Φ_{L_1} and Φ_{L_2}. $L_1 = 39$ and $L_2 = 45$ ($|L_1 - L_2| = 6$). The compact CF wave function at $L = 45$ coincides with the Laughlin trial function.[2] The formation of a pinned (nonrotating) EM representing a (0,6) molecular configuration is transparent. $\alpha = \beta = 1/\sqrt{2}$. Note that all six humps of localized electrons are visible in the electron densities of the pinned CFs (in contrast to five visible humps in the CPDs in Fig. 16). Lengths in units of l_B. The units of the vertical axis are $10^{-2} l_B^{-2}$. The electron density is normalized to the number of particles, N.

with k_q, $q = 1, \ldots, r$ being nonnegative integers.

A central property of these trial functions is that identically

$$\Phi_{\mathcal{L}}^{\mathrm{REM}}(n_1, n_2, \ldots, n_r)[z] = 0 \tag{A4}$$

when

$$\mathcal{L} \neq L_m \tag{A5}$$

This selection rule follows directly from the point group symmetries of the $(n_1, n_2, \ldots, n_r)$ multi-ring polygonal configurations. Indeed under condition (A5) the $C(\ldots)$ coefficients are identically zero. In other words, purely rotational states are allowed only for certain angular momenta that do not conflict with the intrinsic molecular point-group symmetries.

Appendix B: Intrinsic crystalline correlations in composite-fermion wave functions for $\nu > 1/5$

Another class of trial functions that have been shown to approximate well (in energy) the EXD yrast cusp states are the composite-fermion ones;[13] here we refer in particular to the compact[11] (also referred to[52] as mean-field) ones. For larger fractional fillings ($\nu > 1/5$, including $\nu = 1/3$), it has been ascertained[12,13] that the compact CF functions represent paradigms of liquid states devoid of any intrinsic crystalline correlations. Since for $N = 6$ electrons $\nu \geq 1/5$ corresponds to angular momenta $L \leq 75$, the CF CPDs (for $L = 30$ and $L = 39$) displayed in Fig. 16, however, disagree with the above assertion. (The CF wave functions were calculated according to Sec. 4.3 of Ref. 53.) Indeed, well formed crystalline correlations corresponding to the (1,5) molecular isomer (commensurate with a magic angular momentum $L = 30$) and the (0,6) molecular isomer (commensurate with a magic angular momentum $L = 39$) are present in these CF CPDs. This is in agreement with the finding in Ref. 20 that all LLL functions with good L are equivalent to rotating and vibrating Wigner molecules.

The above suggests that the superposition of CF wave functions should also yield pinned Wigner crystallites. This conclusion is explicitly confirmed in Fig. 17, where the electron density (showing well developed crystalline oscillations) of a pinned CF state is displayed for a case in the neighborhood of $\nu = 1/3$ [i.e., for a state constructed by mixing the compact CF states for $L_1 = 39$ and $L_2 = 45$, see Eq. (14)]. We note that the compact CF state for $N = 6$ and $L = 45$ coincides with the Laughlin trial function.[2] We further note that $L_1 - L_2 = 6$, and that accordingly the crystalline configuration in Fig. 17 corresponds to the (0,6) classical molecular isomer. This demonstrates that the selection rules for formation of Wigner crystallites (discussed at the end of Sec. III) apply to the CF trial functions as well.

* Constantine.Yannouleas@physics.gatech.edu
† Uzi.Landman@physics.gatech.edu

[1] D. C. Tsui, H. L. Stormer, and A. C. Gossard, Phys. Rev. Lett. **48**, 1559 (1982).
[2] R. B. Laughlin, Phys. Rev. Lett. **50**, 1395 (1983).
[3] H. Fukuyama and P. A. Lee, Phys. Rev. B **18**, 6245 (1978).
[4] K. Maki and X. Zotos, Phys. Rev. B **28**, 4349 (1983).
[5] Liquid-to-solid (Wigner crystal) crossover as a function of electron density has been discussed, using different variational wave functions for the two phases, for the two-dimensional electron gas in the absence of a magnetic field; see B. Tanatar and and D. M. Ceperley, Phys. Rev. B **39**, 5005 (1989).
[6] P. K. Lam and S. M. Girvin, Phys. Rev. B **30**, 473 (1984).
[7] E. Y. Andrei, G. Deville, D. C. Glattli, F. I. B. Williams, E. Paris, and B. Etienne, Phys. Rev. Lett. **60**, 2765 (1988).
[8] C.-C. Li, J. Yoon, L. W. Engel, D. Shahar, D. C. Tsui, and M. Shayegan, Phys. Rev. B **61**, 10905 (2000).
[9] P. D. Ye, L. W. Engel, D. C. Tsui, R. M. Lewis, L. N. Pfeiffer, and K. West, Phys. Rev. Lett. **89**, 176802 (2002).
[10] Y. P. Chen, R. M. Lewis, L. W. Engel, D. C. Tsui, P. D. Ye, Z. H. Wang, L. N. Pfeiffer, and K. W. West, Phys. Rev. Lett. **93**, 206805 (2004).
[11] J. K. Jain, Phys. Rev. Lett. **63**, 199 (1989)
[12] J. K. Jain, Physics Today **53**, 39 (2000); *The Composite Fermion,* http://www.phys.psu.edu/ jain/cf.html
[13] J. K. Jain, *Composite Fermions* (Cambridge University Press, Cambridge, England, 2007).
[14] H. Yi and H. A. Fertig, Phys. Rev. B **58**, 4019 (1998).
[15] R. Narevich, G. Murthy, and H. A. Fertig, Phys. Rev. B **64**, 245326 (2001).
[16] C-C. Chang, G. S. Jeon, and J. K. Jain, Phys. Rev. Lett. **94**, 016809 (2005).
[17] C-C. Chang, C. Töke, G. S. Jeon, and J. K. Jain, Phys. Rev. B **73**, 155323 (2006).
[18] H. Zhu, Y. P. Chen, P. Jiang, L. W. Engel, D. C. Tsui, L. N. Pfeiffer, and K. W. West, Phys. Rev. Lett. **105**, 126803 (2010).
[19] H. Zhu, G. Sambandamurthy, Y. P. Chen, P. Jiang, L. W. Engel, D. C. Tsui, L. N. Pfeiffer, and K. W. West, Phys. Rev. Lett. **104**, 226801 (2010).
[20] C. Yannouleas and U. Landman, Phys. Rev. A **81**, 023609 (2010).
[21] C. Yannouleas and U. Landman, Phys. Rev. B **66**, 115315 (2002).
[22] C. Yannouleas and U. Landman, Phys. Rev. B **68**, 035326 (2003).
[23] C. Yannouleas and U. Landman, Phys. Rev. B **70**, 235319 (2004).
[24] C. Yannouleas and U. Landman, Rep. Prog. Phys. **70**, 2067 (2007).
[25] The effects of disorder (pinning) at zero magnetic field in stabilizing the Wigner crystal against the liquid phase, resulting in a shifting of the crossover between these phases to higher electron densities, have been discussed in T. Chui and B. Tanatar, Phys. Rev. Lett. **74**, 458 (1995). Impurity pinning effects of Wigner molecules (by both attractive and repulsive impurities) have been studied theoretically in the context of electrons confined in 2D semiconductor quantum dots; for magnetic-field-free conditions (for up to eight electrons), see C. Yannouleas and U. Landman, Phys. Rev. B **61**, 15895 (2000), and for a study with an applied magnetic field (for $N = 3$ and $N = 4$ electrons), see B. Szafran and F. M. Peeters, Europhys. Lett. **66**, 701 (2004).
[26] J. K. Jain and T. Kawamura, Europhys. Lett. **29**, 321 (1995).
[27] Yuesong Li, C. Yannouleas, and U. Landman, Phys. Rev. B **73**, 075301 (2006).
[28] K. Takano and A. Isihara, Phys. Rev. B **34**, 1399 (1986).
[29] X. Wan, K. Yang, and E. H. Rezayi, Phys. Rev. Lett. **88**, 056802 (2002).
[30] O. Ciftja and C. Wexler, Phys. Rev. B **67**, 075304 (2003).
[31] X. Wan, E. H. Rezayi, and K. Yang, Phys. Rev. B **68**, 125307 (2003).
[32] S. Jolad and J. K. Jain, Phys. Rev. Lett. **102**, 116801 (2009).
[33] S. Jolad, D. Sen, and J. K. Jain, Phys. Rev. B **82**, 075315 (2010).
[34] S. M. Girvin and T. Jach, Phys. Rev. B **28**, 4506 (1983).
[35] Vibrational excitations of a similar form, i.e.,

$$\tilde{Q}_\lambda = \sum_{i=1}^{N} z_i^\lambda \tag{B1}$$

(and certain other variants), have been used earlier than Ref. 20 to approximate *part* of the LLL spectra. Such earlier endeavors provided valuable insights, but overall they remained inconclusive; for electrons over the maximum density droplet [with magic $L_m = L_0$], see M. Stone, H. W. Wyld, and R. L. Schult, Phys. Rev. B **45**, 14 156 (1992) and J. H. Oaknin, L. Martín-Moreno, J. J. Palacios, and C. Tejedor, Phys. Rev. Lett. **74**, 5120 (1995); for electrons over the $\nu = 1/3$ Jastrow-Laughlin trial function [with magic $L_m = 3L_0$], see J. J. Palacios and A. H. MacDonald, Phys. Rev. Lett. **76**, 118 (1996); and for bosons in the range $0 \leq L \leq N$, see B. R. Mottelson, Phys. Rev. Lett. **83**, 2695 (1999) and Th. Papenbrock and G.F. Bertsch, Phys. Rev. A **63**, 023616 (2001). The advantage of Q_λ (compared to $\tilde{Q}_\lambda$) is that it is translationally invariant,[20] a property shared with $\Phi_{\mathcal{L}}^{\rm REM}$.
[36] The RVEM diagonalization provides a unified molecular treatment that can also be applied to an assembly of N bosons in the LLL, as shown in Ref. 20.
[37] For higher angular momenta, the cusp states progressively correspond exlusively to the (1,5) ring configuration, which classically is the most stable one; see Ref. 22.
[38] V. M. Bedanov and F. M. Peeters, Phys. Rev. B **49**, 2667 (1994).
[39] M. Kong, B. Partoens, and F. M. Peeters, Phys. Rev. E **67**, 021608 (2003).
[40] W. Y. Ruan, Y. Y. Liu, C. G. Bao, and Z. Q. Zhang, Phys. Rev. B **51**, 7942 (1995).
[41] T. Seki, Y. Kuramoto, and T. Nishino, J. Phys. Soc. Jpn. **65**, 3945 (1996).
[42] P. A. Maksym, Phys. Rev. B **53**, 10871 (1996).
[43] M. B. Tavernier, E. Anisimovas, F. M. Peeters, B. Szafran, J. Adamowski, and S. Bednarek, Phys. Rev. B **68**, 205305 (2003).
[44] E. V. Tsiper and V. J. Goldman, Phys. Rev. B **64**, 165311 (2001).
[45] Deviations of the same nature (i.e., overestimation of the

vibrational components) between the EXD and Laughlin-state radial EDs have been reported for the whole range $5 \leq N \leq 12$ of LLL electrons (see Ref. 44); these deviations increase slowly with increasing N.

[46] For a $(0, N)$ configuration, the magic angular momenta L_m are given by $L_m = L_0 + kN$, $k = 0, 1, 2, \ldots$ [for L_0 see Eq. (3)]; i.e., for $N = 6$: $L_m = 15$, 21, 27, 33, 39, 45, 51, ... Similarly, for a $(1, N-1)$ configuration, $L_m = L_0 + k(N-1)$ $(k = 0, 1, 2, \ldots)$, giving for $N = 6$: $L_m = 15$, 20, 25, ..., 40, 45, 50, ...

[47] Any nonrotating (static) electron-molecule state is a wave packet, and thus it is expandable in a complete basis of rotating electron molecule states with good total angular momenta. Therefore, given the wave function of the nonrotating EM, a state with good total angular momentum can be obtained from it via an appropriate projection. This constitutes the direct projection method developed by us in the context of "restoration of broken symmetries" (see Refs. 21, 22, and 24). The term "reverse projection" is used to indicate the "inverse" operation to the direct projection, namely, the method of generating the wave function of a nonrotating EM out of the states (with good angular momentum) of a rotating and vibrating electron molecule.

[48] M. O. Goerbig, P. Lederer, and C. Morais Smith, Phys. Rev. Lett. **93**, 216802 (2004).

[49] M. O. Goerbig, P. Lederer, and C. Morais Smith, Phys. Rev. B **69**, 115327 (2004).

[50] In addition to the second-half (starting with "Both liquid and solid phases ...") of the introductory paragraph in Ref. 48, the inapplicability of the Hamiltonian CF approach to filling-factor ranges around integer values can be explicitly traced to Ref. 49; see in particular the sentence "We further require that the partial filling factor of the last level $\bar{\nu} = \nu - [\nu]$ is different from zero because at integral fillings, the only possible low-energy excitations are inter-LL excitations, which cost an energy of order $\hbar\omega_c$ ..." in the first paragraph of Sec. II therein.

[51] An attempt to formulate a variant of a CF Wigner crystal, referred to simply as CFC, for a finite number of electrons N was presented in Refs. 16 and 17. This CFC formulation, however, is explicitly inapplicable to the $\nu = 1/3$ neighborhood; see Sec. 15.2 (p. 450) in Ref. 13.

[52] G. S. Jeon, C. C. Chang, and J. K. Jain, Eur. Phys. J. B **55**, 271 (2007).

[53] J. K. Jain and R. K. Kamilla, in *Composite Fermions: A Unified View of the Quantum Hall Regime,* Edited by O. Heinonen (World Scientific, Singapore, 1998).